Geophysical Journal International

Seismic evidence for lithospheric modification associated with intra-continental volcanism in Northeastern China

Journal:	*Geophysical Journal International*
Manuscript ID:	Draft
Manuscript Type:	Research Paper
Date Submitted by the Author:	n/a
Complete List of Authors:	Kang, Dou; Peking University, Institute of Theoretical and Applied Geophysics, School of Earth and Space Sciences Shen, Weisen; University of Colorado at Boulder, Department of Physics Ning, Jie-yuan; Peking University, Institute of Theoretical and Applied Geophysics, School of Earth and Space Sciences Ritzwoller, Michael; University of Colorado at Boulder, Department of Physics
Keywords:	Surface waves and free oscillations < SEISMOLOGY, Seismic tomography < SEISMOLOGY, Asia < GEOGRAPHIC LOCATION, Crustal structure < TECTONOPHYSICS

Seismic evidence for lithospheric modification associated with intra-continental volcanism in Northeastern China

Dou Kang[1], Weisen Shen[2*], Jieyuan Ning[1], and Michael H. Ritzwoller[2]
1 - Institute of Theoretical and Applied Geophysics, School of Earth and Space Sciences, Peking University, Beijing, 100871, China
2 - Department of Physics, University of Colorado at Boulder, Boulder, CO 80309, USA
weisen.shen@colorado.edu

Abstract

Using data predominantly from the NECESS Array, but also incorporating surface wave data from surrounding networks, we present the results of a Bayesian Monte Carlo inversion of receiver functions, Rayleigh wave ellipticity (H/V ratio), and Rayleigh wave group and phase speeds from 8-80 sec period for the 3D shear velocity structure of the crust and uppermost mantle beneath Northeast China. We define the final model as the mean and standard deviation of the posterior distribution at each location on a 0.5°x0.5° grid from the surface to 150 km depth. The primary scientific motivation is to investigate the expression of intra-continental volcanism across the region. The model lithosphere displays prominent features (middle and lower crustal velocity, Moho depth, lithospheric thickness) across the study area that coincide with the locus of volcanoes, which are predominantly situated in two distinct volcanic regions, which we call the "Northeast China Lineated Quaternary Volcanic Zone", found near the eastern margin of the Songliao Basin and extending to Changbaishan Volcano, and the "Northern and Southern Greater Xing'an Range Pleistocene Volcanic Zones". There is a strong similarity between the lateral distribution of depth-integrated mantle velocity anomalies in our model with the teleseismic body wave model of Tang et al. (2014), although the vertical distribution of anomalies differ.

Key words: Surface waves and free oscillations; Receiver functions; Seismic tomography; Joint inversion; Crustal structure; Mantle structure; China; Volcanism

1. Introduction

In a recent study, Shen et al. (2015) produced a seismic reference model of shear wave speeds in the crust and uppermost mantle across China, as a continuation and culmination of three earlier studies (Yang et al., 2010, 2012; Zheng et al., 2011; Zhou et al., 2012). This model, which we refer to here as China_2015, was produced using measurements of Rayleigh wave dispersion alone that derived from ambient noise and earthquake tomography. China_2015 is principally a Vs model, and is presented on a 0.5°x0.5° degree grid across all of China, extending to a depth of 150 km. The model was generated via a Bayesian Monte Carlo inversion and is defined by the mean and standard deviation of the posterior distribution at each grid node. Such surface wave inversions characterize Vs between discontinuities much better than the depths to interfaces, and Shen et al. (2015) present their model (and the group and phase speed maps on which it was derived) specifically to act as the basis for later studies that incorporate data that complement information from surface wave dispersion. The purpose of the present paper is to refine the model of the crust and uppermost mantle in northeastern China beneath the NECESS Array (NorthEast China Extended SeiSmic Array) by introducing two additional types of data: receiver functions and Rayleigh wave ellipticity (or H/V ratio). These data provide much tighter constraints on sedimentary and crustal thicknesses than surface wave dispersion alone, which improves depth resolution in the model substantially. To the best of our knowledge, this is the first study to invert surface wave dispersion, receiver functions, and H/V ratio simultaneously.

Our study focuses on the use of data from the NECESS experiment, which deployed 127 temporary broadband seismometers, with the average station spacing of ~ 80 km, across Northeast China from September 2009 to August 2011. The array ranges from about 116° to 134°E in longitude and 42° to 48°N in latitude, covering part of the Erlian basin (ELB), most of the Greater Xing'an Range (GXAR), the Songliao basin (SLB), the Zhangguangcai Range (ZGCR), the Changbai Mountain Range (CBM), the Sanjiang basin (SJB) and the Jiamusi Massif, as illustrated in Figure 1b. The unprecedented station coverage provided by the NECESS Array (e.g., Tang et al., 2014; Tao et al., 2014) motivates us to develop multiple seismic datasets to illuminate the seismic structure of the lithosphere in Northeast China. We produce receiver functions (RF) from all 127 stations, while we obtain Rayleigh wave measurement (both dispersion and ellipticity) for 120 stations for which we have instrument response information.

The model we present here is constructed with a joint Bayesian Monte Carlo inversion of Rayleigh wave phase and group velocities, receiver functions, and measurements of the period-dependent Rayleigh wave H/V ratio (Lin et al., 2012; Lin et al., 2014). The surface wave dispersion data are the same as those used by Shen et al. (2015) to construct the reference model China_2015. These data include ambient noise and earthquake tomography maps in northeastern China from a wide variety of data sources including the GSN, NECESS, F-Net (in Japan), CEArray, and the Korean Seismic Network. The Rayleigh wave dispersion measurements from earthquakes incorporated in that model, however, were actually processed for the present study and we discuss them here at greater length. Shen et al. (2015) used measurements, maps, and uncertainties of Rayleigh wave phase speed from 30 sec – 70 sec period derived from the application of Helmholtz tomography and we further add results at 75 sec and 80 sec. We construct the receiver functions using a revision of the harmonic stripping method described by Shen et al. (2013a,b), where the revision is motivated by the azimuthal content of the receiver functions in this region. The inversion method we apply is also a straightforward generalization of the method described at length by Shen et al. (2013a). Because the data we use overlap the data used to produce the reference model China_2015, in order for a more meaningful comparison we do not use that model as our starting point but rather the earlier model of Zheng et al. (2011), which was also the starting point for the reference model China_2015.

Northeast China principally is composed of geological terranes that were amalgamated during the Paleozoic and Mesozoic Eras (Wu et al., 2011). The region underwent active intra-continental magmatism and extension during the late Mesozoic era (Ren et al., 2002; Wang et al., 2006), which led to Basin and Range type fault basins, including the NNE-trending Songliao Basin which lies at the center of our study region (Ren et al., 2002; Wei et al., 2010; Feng et al., 2010). Consensus has yet to be reached regarding the nature of the intraplate volcanism and its relation to deeper geodynamic processes, although various models have been proposed; e.g., mantle plume (e.g., Lin et al., 1998), back-arc extension associated with the subduction and rollback of the Paleo-Pacific plate (e.g., Watson et al., 1987; Wei et al., 2010) and delamination of the thickened lithosphere after closure of the Mongol-Okhotsk Ocean (e.g., Wang et al., 2006; Zhang et al., 2010). In the Cenozoic Era, northeastern China experienced several additional episodes of volcanism, which initiated in the Songliao graben and then migrated flankward (Liu et al., 2001). The locations and approximate ages of the principal Cenozoic volcanoes in our study region are identified in Figure 1a (Chen et al., 2007), where we identify two distinct volcanic regions, which we call the "Northeast China Lineated Quaternary Volcanic Zone" and the "Northern and Southern Greater Xing'an Range Pleistocene Volcanic Zones".

The primary motivation of this study is to investigate the expression of intracontinental volcanism in the crust and uppermost mantle beneath Northeast China. The model we present is not the first model of the crust and uppermost mantle beneath Northeast China. Earlier surface wave models include those of Zheng et al. (2011) and Shen et al. (2015) as well as others (Huang et al., 2003; Zheng et al., 2008; Li et al., 2012; Li et al., 2013; Bao et al., 2015), and some studies have combined surface wave with other data (Obrebski et al., 2012; Guo et al., 2014). However, the model presented here possesses several signature novelties. (1) It is based an extensive surface wave dispersion data set using both ambient noise and earthquake tomography that is equaled only by the study of Shen et al. (2015). (2) It incorporates two sources of complementary information about shallow structures as well as depths to interfaces: receiver functions and Rayleigh wave H/V ratios. (3) The model that we present possesses uncertainty estimates, which we contrast with uncertainty estimates using surface wave data alone to demonstrate the advantage of the new measurements. Finally, we compare our results in the mantle with the teleseismic body wave model of Tang et al. (2014), which is also based on the use of NECESS data.

The paper is organized as follows. In section 2 we discuss the development of the Rayleigh wave phase and group velocity data sets from both ambient noise and earthquake data, the Rayleigh wave H/V data set, and the receiver function data set, including quality control procedures and observational uncertainties. In section 3 we discuss the inverse problem including model parameterization, the generation of the prior distribution, and a detailed assessment of the affect of introducing receiver functions and H/V data on the posterior distribution. Section 4 discusses the resulting model and uncertainties, defined as the mean and standard deviation of the posterior distribution at each point, respectively. Finally, in section 5 we describe the resulting model and discuss it.

2. Data Processing

2.1 Correction of Sensor Misorientation

Measurements of receiver functions and surface wave polarization require the rotation of the two horizontal components, but seismometer misorientation may bias the results. We estimate the component azimuths for each NECESS Array station by analyzing the particle motions of teleseismic *P*-waves using the method of Niu and Li (2011). We collect earthquakes with magnitudes greater than 5.5 in the epicentral distance range from 30°-90° with signal-to-noise ratios (SNR) larger than 5. For each station, we compare the back-azimuth of each event with the horizontal projection of the *P*-wave polarization direction to estimate the misorientation. We average all estimates from earthquakes with consistent results and find that the average misorientation is small, meaning that there is little bias in the orientations, on average. However, there are six stations with misorientation azimuths ≥10°. We correct the orientations for these six stations and discard seven other stations for which the orientation estimates are not stable over time. We do not correct misorientations less than 10° because below this level they may be caused by near station structures and will not affect our results significantly (Niu and Li, 2011). The standard deviation of the misorientations after we correct the six stations and discard the other seven stations is 3.3° and the mean misorientation is -0.1°.

2.2 Rayleigh Wave Ellipticity (H/V Ratio)

We use earthquakes with Mw ≥ 5.0 (ISC catalogue) between September 2009 and March 2011, and from the NEIC PDE catalogue between March 2011 and August 2011, which yields a total of 3734 events. After correcting sensor misorientations (Section 2.1), we rotate the seismograms to get the radial and transverse components. For each earthquake, we apply automated frequency-time analysis (FTAN) at each station (Bensen et al., 2007) to measure the Rayleigh wave amplitudes on both vertical and radial components as well as the group and phase travel times. The H/V ratio measurements (the amplitude ratio of the radial and vertical components) are then obtained at periods between 20 sec and 80 sec.

For each station and each period T, we follow Lin et al. (2012) to measure H/V but impose more strict criteria based on the data quality to ensure the reliability of the measurements. (1) We only keep those measurements with SNR larger than 15 on both radial and vertical components. (2) We require that the phase and group traveltimes measured on the radial and vertical components are consistent (i.e., $|tt_{ph\_R}-tt_{ph\_Z}-T/4| \leq 8/T$ and $|tt_{gr\_R}-tt_{gr\_Z}| \leq 10$ s, where tt_{ph_R} and tt_{ph_Z} are phase travel times on the radial and vertical components, and tt_{gr_R} and tt_{gr_Z} refer to the group travel times). (3) We set the upper limit value of H/V to be 5. (4) We then take the average of all measurements from different earthquakes, remove 2σ outliers, and repeat this step once. If more than 20 measurements pass the above criteria, we use the mean and the standard deviation of the mean of these measurements as the H/V ratio and its uncertainty at each period. There are, for example, on average ~180 earthquakes that pass the above criteria at 24 s period and ~90 earthquakes at 40 s period. Because the uncertainties may be somewhat underestimated, we follow Lin et al. (2014) and scale them up by a factor of 2 to provide a more realistic estimate for the later inversion (See Section 2.2.2).

We identify six stations that have abnormal amplitude responses based on the H/V measurements. For each period, the H/V measurements at each station should be stable over time. However, for station NE3A, we observe that the measured H/V ratio increases by a factor of two during its deployment. This may be caused by the loss of the differential output of the vertical component of the seismograph. At station NE52, the H/V ratio is too low compared to nearby stations. At the other four stations, the H/V ratio measurements from a group of earthquakes that occurred in March 2011 show inconsistent high values. The reason for this problem is unknown and requires further investigation. We discard the measurements during suspicious abnormal time periods at these stations for both the H/V ratio and the following RF analysis (See Section 2.4).

The H/V ratio is particularly sensitive to the Vs structure in the upper few kilometres even at long periods (Lin et al., 2012). The estimated H/V ratio at 24 and 40 sec period are shown in Figure 2. The observed H/V ratios show clear correlations with geological features. High H/V ratios are observed in sedimentary basins (e.g., the Songliao, Erlian, and Sanjiang basins) and low H/V ratios in mountain ranges (e.g., the Greater Xing'an Range, the Zhangguangcai Range, and the Changbai Mountain Range). For the Songliao Basin, the central basin area and the Kailu depression in the southwest possessing relatively thick sedimentary fill are also clearly delineated by high H/V ratios. The estimated H/V ratio uncertainties at 24 and 40 s are generally smaller than 3% of the estimated value, which is comparable to that measured beneath the USArray (Lin et al., 2014).

Examples of estimated H/V curves for stations NE53 and NE8C are shown in Figure 3b,e. Station NE53 lies in the Greater Xing'an Range west of the Songliao Basin and station NE8C lies in the Songliao Basin (Fig. 1b). The curves are quite different. The higher values at NE8C are characteristic of sedimentary basins.

2.3 Rayleigh Wave Dispersion

2.3.1 Earthquake tomography (ET)

We apply Helmholtz tomography (Lin and Ritzwoller, 2011) to Rayleigh wave measurements from the earthquake data set discussed in Section 2.2 (compiled for H/V measurements) to determine Rayleigh wave phase velocity maps from 30 s to 80 s period on a 0.2°×0.2° grid. For each earthquake and wave period, frequency-time analysis (FTAN) is applied to measure the Rayleigh wave amplitudes and phase travel times on the vertical component at each station. Phase velocities at each location are then determined locally by calculating the gradient of the traveltime field and the Laplacian of the amplitude field (the finite frequency correction term). We discard all measurements with Rayleigh wave SNR less than 8. Following Lin and Ritzwoller (2011), the 2π phase ambiguity is resolved and measurements from particular earthquakes are discarded following criteria based on the curvature of the phase travel time and amplitude surfaces across the array. We only obtain results at locations where there are measurements from more than 50 earthquakes. On average, measurements from about 350 earthquakes are used at each location at 30 sec period and 110 earthquakes at 70 sec period. We then calculate the mean and the standard deviation of the mean over all measurements from different earthquakes to estimate the isotropic phase velocity and its uncertainty at each location.

In contrast with eikonal tomography, Helmholtz tomography takes into account the finite frequency effect by introducing an amplitude dependent correction term, which tends to reduce both random as well as systematic errors (Lin and Ritzwoller, 2011). We find that the average uncertainties for the isotropic phase velocity maps after the finite frequency correction are reduced. A comparison of the isotropic phase velocity maps with (Helmholtz tomography) and without (eikonal tomography) the finite frequency correction at 60 sec period is shown in Figure 4. The standard deviation of the differences between the isotropic phase velocity maps from Helmholtz and eikonal tomography is 7 m/s at 40 sec and 16 m/s at 60 sec period, consistent with the expectation that the magnitude of the finite frequency correction increases with period.

Raw uncertainty estimates in Helmholtz/eikonal tomography are usually underestimated (e.g. Lin et al., 2009) for two reasons: individual measurements at particular locations and periods are not entirely independent (Shen et al., 2015). Following Xie et al. (2015) and Lin et al. (2009), the uncertainties in the isotropic maps are scaled up (by a factor of 2 in this study) to encompass the differences between the ambient noise and earthquake tomography maps. Shen et al. (2015) describe and document this process in detail, and assimilate the measurements we obtain in their study. These measurements, therefore, have been included in the reference model China_2015.

2.3.2 Ambient noise tomography (ANT)

We assimilate group and phase velocity measurements from ambient noise tomography (from 8 sec to 50 sec period) from the earlier study of Shen et al. (2015). These data are the basis for the reference model China_2015. This study applied the straight ray tomography method of Barmin et al. (2001) to produce isotropic Rayleigh wave group and phase velocity maps on a 0.5°×0.5° grid that extends well outside our study area. Examples of Rayleigh wave phase velocity maps are presented in Figure 5 at periods of 10 sec, 20 sec, 30 sec, and 40 sec from ambient noise tomography as well as at 40 sec from earthquake tomography. The ambient noise maps extend throughout China. Azimuthal anisotropy was estimated simultaneously to minimize anisotropic bias in the dispersion maps. Uncertainties were estimated based on Helmholtz/eikonal tomography with extension to areas where these methods were not applied based on lateral resolution.

2.3.3 Construction of group and phase velocity curves at each station

We produce Rayleigh wave group and phase velocity maps every 2-sec-period from 8 sec to 32 sec and then every 5-sec-period from 35 sec to up to 80 sec. For the ambient noise map, we only keep the measurements at those locations where the resolution is better than 160 km. Uncertainties in the ambient noise and earquake derived maps are discussed by Shen et al. (2015). We merge the ambient noise and earthquake tomography maps together with their uncertainties and generate maps on a 0.5°×0.5° grid. At short periods (8 sec - 30 sec), phase velocity maps are produced based on ambient noise alone; while at long periods (50 sec - 80 sec) only earthquake tomography maps are used. In the period band of overlap (30 sec - 50 sec), we average the phase velocity measurements and the uncertainties locally from the ambient noise and earthquake tomography maps, weighting up the ambient noise tomography maps at shorter periods and the earthquake based maps at longer periods. Examples of Rayleigh wave phase speed maps at 40 sec period based on ambient noise and earthquake data are presented in Figure 5d,e. Shen et al. (2015) argue that the differences between these maps, with a standard deviation of 27 m/s, are within the stated uncertainties. We then interpolate the phase velocities from a regular grid to each station location. Phase velocity curves at each station are constructed by averaging the velocities at the nearby grid points (distance < 0.6°), taking the Gaussian function of the distance as the weight. The group velocity curves are derived only from the ambient noise maps and extend from 8 s to 50 s.

Figure 3c,f shows examples of Rayleigh wave group and phase speed curves and uncertainties (presented as one standard deviation error bars) for two sample stations: NE53 and NE8C, whose locations identified in Figure 1b. As with the Rayleigh wave H/V ratios at these stations, the dispersion curves for at two stations differ appreciably; for example, group speed at short periods is much lower beneath the Songliao Basin.

2.4 Receiver Function Data Processing

We use teleseismic *P*-wave data from earthquakes with Mw ≥ 5.0 and epicentral distances within 30°-95° from the centre of the array (total 1970 events) to produce radial component *P*-wave receiver functions (RFs). After the sensor misorientation correction (Section 2.1), we rotate the seismograms to get the radial and transverse components and apply the time-domain iterative deconvolution method (Ligorria and Ammon, 1999), choosing a time window of [-20 s, 60 s] relative to the direct *P*-wave arrival time. A low-pass Gaussian filter with the width factor of 3 (pulse width ~1 s) is used to suppress high-frequency noise in the RFs. Move-out corrections of both the time and amplitude of RFs are made to a reference slowness of 0.06 s/km based on the *Ps* phase generated from the *P*-to-*S* conversions off Moho.

Following Shen et al. (2013a), we impose several selection criteria. (1) Based on the analysis of Section 2.1, the estimated component azimuths from analyzing the particle motions of teleseismic *P*-waves should be stable over time. We find, however, that 30 stations show inconsistency in the estimated component azimuths during some time periods, among which seven are identified as erroneous stations with possible instrument errors because the estimated component azimuths scatter during the entire deployment time. This may result from abnormal instrument responses. We discard the RFs during such suspicious abnormal times before further analysis. Note that the criteria we impose on the H/V ratio measurements already have largely eliminated the measurements during the suspicious abnormal times, so we do not apply this additional quality control to H/V ratio measurements, except for rejection of these seven erroneous stations. (2) As discussed in Section 2.2, we also discard the RFs during suspicious abnormal time periods recognized by the H/V ratio analysis. (3) Only those RFs that produce a match between the radial and vertical components greater than 80% in the iterative deconvolution process are used in later analyses. (4) We delete RFs with abnormal values: the amplitude of RFs should be less than 1 and the value at zero time should be positive. (5) We further remove inconsistent RFs by comparing them with the RF averaged over back-azimuthal groups (the 2-norm distance should be less than 0.1). On average, about 160 RFs are selected for each station.

Shen et al. (2013a,b) proposed the "harmonic stripping" method in which raw single-event RFs that pass quality control are fit by a truncated harmonic function $H(\theta,t)$ as follows:

$$H(\theta,t) = A_0(t) + A_1(t)\sin[\theta+\theta_1(t)] + A_2(t)\sin[2\theta+\theta_2(t)] \quad (1)$$

where $H(\theta,t)$ is called the estimated RF. The fitting is done to estimate the azimuthally independent component $A_0(t)$ which represents the azimuthally isotropic average of the structure beneath the receiver. Examples of the raw RFs, the estimated RFs $H(\theta,t)$, and the harmonic component $A_0(t)$, $A_1(t)$, and $A_2(t)$, are presented in Figure 6. This figure demonstrates an important characteristics of RFs in Northeast China; namely, that the vast majority of earthquakes lie in the azimuthal range from 120° to 240°, lying in the range from the southeast to the southwest of each station. (More than 75% of the events are within this back-azimuth range.) When the back-azimuthal coverage of the RFs is sparse, $A_0(t)$ may not provide a good estimate of local azimuthally independent structure. For this reason, we modify the harmonic stripping method. Instead of using $A_0(t)$ as the azimuthally independent RF, we average $H(\theta,t)$ between 120° and 240° azimuth and find that this provides a more repeatable and reliable representation of local isotropic structure.

As an estimate of uncertainty, we compute the RMS difference between $H(\theta,t)$ and the observed RFs and use it as the 1σ uncertainty of the average estimated RF at each time. We believe that the uncertainties estimated in this way are somewhat overestimated (Shen et al., 2013a); therefore we scale them down by a factor of 2 to compensate. If uncertainties are unreasonably low (less than 0.02), we enlarge them to 0.02. We also double the uncertainties for nine stations if the number of raw RFs that pass the above criteria is less than 10 or the quality of RF is relatively low.

Finally, for stations showing particularly strong azimuthal variations, which we attribute to the effect of laterally varying structures, we choose an even narrower back-azimuthal range (120° to 180° or 180° to 240°) in which we average the RFs. This is performed at 13 stations. For these stations, the average RFs from different back-azimuthal groups show different features, which means that simply stacking them together will not represent average structure near the station. In this case we choose the back-azimuthal range where the RFs appear more representative of local structure and more in agreement with the parameterization we use to fit our model. For example, if receiver functions in an azimuthal sub-range present evidence for a strong mid-crustal discontinuity we are likely to choose another range that does not present such evidence.

Example receiver functions are shown in Figure 3a,d for stations NE53 and NE8C. As with the dispersion data and the H/V measurements, they are quite different. The receiver function at station NE8C displays reverberations caused by sediments in the Songliao Basin which obscures the *Ps* converted phase at the Moho, while the receiver function at station NE53 in the Greater Xing'an Range displays a prominent converted phase. Receiver functions such as the one shown in Figure 3d, which display strong reverberations due to sediments, are commonly viewed in receiver function studies as non-informative because they do not provide strong constraints on crustal thickness. However, in our joint inversion, such receiver functions are enormously useful because they provide strong constraints on sedimentary velocities and and thickness.

3. Joint Inversion of Rayleigh Wave Ellipticity (H/V), Rayleigh Wave Dispersion and Receiver Functions (RFs)

Surface wave phase and group speeds are sensitive to the averaged Vs velocities over depths based on their sensitivity kernels, which deepen with period, but weakly constrain discontinuity depths or velocity jumps across the discontinuities. Receiver functions, in contrast, serve as a good complement to surface wave dispersion due to the information they provide about velocity contrasts. The joint inversion of surface wave dispersion and receiver functions has evolved to become a more effective means to resolve crustal and upper mantle structure than inversions based on either data set alone (e.g. Julià et al., 2000; Bodin et al., 2012; Shen et al., 2013a, b). Rayleigh wave ellipticity, or H/V (horizontal-to-vertical) ratio, is particularly sensitive to very shallow earth structure (e.g. Boore and Nafi Toksöz, 1969; Tanimoto and Rivera, 2008; Yano et al., 2009). Recently, Lin et al. (2012) demonstrated that intermediate to long-period H/V ratio measurements of earthquake surface wave signals are robust and compatible with traditional phase velocity measurements and can be used together with dispersion measurements to improve the resolution of crustal structures, especially in the several kilometers directly beneath the surface. In this study, we apply a non-linear Bayesian Monte-Carlo algorithm (Shen et al., 2013a) to estimate V_S structure by jointly interpreting Rayleigh wave velocities, RFs and Rayleigh wave ellipticity data. To the best of our knowledge, this is the first study to use these three data sets simultaneously.

3.1 Model Parameterization

Because Rayleigh waves are primarily sensitive to vertically polarized shear wave speeds (Vsv) rather than horizontally polarized shear wave speeds (Vsh), here we assume an isotropic Vsv model where Vs = Vsh = Vsv. RFs are used from 0-10 s and the longest period of surface waves that we use is 80 sec, which provides reliable information about the top 150 km of the crust and uppermost mantle. We invert for a local 1-D model beneath each station rather than on a regular grid, and form the 3-D model by compiling the complete set of 1-D models. Following Shen et al. (2013a, b), we impose a smooth parameterization vertically between interfaces.

The 1-D model beneath each station is parameterized with three principal layers: a sedimentary layer with a linear velocity gradient with depth, a crystalline crustal layer, and a mantle layer. (1) The sedimentary layer is described by layer thickness and Vsv values at the top and bottom of the layer. (2) The crystalline crustal layer is described by six parameters: layer thickness and five B-splines for Vsv. (3) Mantle structure is modeled from the Moho to 200 km depth with five B-splines for Vsv. We set the V_P/V_S ratio to 2.0 in the sedimentary layer and 1.79 in the mantle based on AK135 (Kennett et al., 1995) and use the scaling relation from Brocher (2005) in the crystalline crustal layer. For density, we use the relation based on Brocher (2005) in the crust and Hacker and Abers (2004) in the mantle. We apply a physical dispersion correction (Kanamori & Anderson 1977) using the Q-model from AK135 in the crust (Kennett et al., 1995) and the global model from Dalton and Ekstrom (2006) in the mantle. The smoothness of the model is imposed by the parameterization so that ad hoc damping is not needed during the inversion (Shen et al., 2013 a,b).

We also find that for some stations located in the basins, we need to add one more unconsolidated sedimentary layer to fit the data, which is also supported by previous RF studies (Tao et al., 2014). For basin stations at which the resulting misfit can be improved by more than 20% (i.e., at 10 stations), we apply another parameterization by adding a thin sedimentary layer with a linear velocity gradient with depth on the top and set the V_P/V_S ratio to 3.0 in this layer (Tao et al., 2014). Most of these locations are in the Songliao Basin, but some are in the Hailar, Erlian, and Sanjiang basins. Stations where there are one or two sedimentary layers are identified in Figure 1b.

3.2 Prior and Posterior Distributions

The model space for Monte Carlo sampling is defined relative to a starting model (Zheng et al., 2011) with perturbations defined in Table 1. For sedimentary basins, we enlarge the sedimentary thickness in the starting model based on previous geological cross sections (Wei et al., 2010; Zhang et al., 2012; Chen et al., 2014). Additional model constraints are imposed: (1) Vs < 4.9 km/s at all depths; (2) velocity increases monotonically with depth in the crystalline crust; (3) the velocity contrasts across the sedimentary basement and the Moho discontinuity are positive (Shen et. al, 2013b). Examples of the prior distribution for particular model variables are presented in Figure 7 as white histograms, and discussed further in section 3.4.

Following the procedure described by Shen et al. (2013a,b), a random walk in the model space is performed guided by the Metropolis algorithm (Mosegaard & Tarantola, 1995). Models are accepted if their misfit is less than 1.5 times that of the best fitting model. The posterior distribution of models is the ensemble of all accepted models and its statistical properties quantify model uncertainties. RMS misfit is the square root of the joint χ^2 misfit, which is defined as follows:

$$\sqrt{\chi^2_{joint}} = 0.5 \cdot \sqrt{\chi^2_{SW}} + 0.5 \cdot \sqrt{\chi^2_{RF}} = 0.5 \cdot \sqrt{\frac{1}{N}\sum_{i=1}^{N}\frac{[g_i(m) - D_i^{obs}]^2}{\sigma_i^2}} + 0.5 \cdot \sqrt{\frac{1}{L}\sum_{i=1}^{L}\frac{[R_i(m) - H(t_i)]^2}{\sigma_i^2}}$$

where $g_i(m)$ is the predicted Rayleigh wave phase or group speed or H/V ratio, $R_i(m)$ is the predicted RF; σ_i is the corresponding one standard deviation uncertainty of the observation; N, L are the number of surface wave measurements (including the phase/group velocities and H/V ratio at different periods) or discrete times in the RF, respectively. Examples of posterior distributions are also presented in Figure 7 as red histograms.

3.3 Fit to the Data

Due to the various data acceptance and rejection issues described in section 2, not all stations have data from the same measurements. The vast majority of stations, 105 in total, have all three data sets: surface wave dispersion, H/V, and RFs. However, 12 stations have only Rayleigh wave dispersion measurements and RFs, 3 stations have dispersion and H/V ratio alone, and 9 stations have only dispersion measurements (Fig. 1b). The RMS misfit of the mean model in the posterior distribution (named as the average accepted model) in the joint inversion is 0.93 on average. If $\chi^2_{joint} \sim 1$ then data uncertainties are appropriately estimated and the model generally possesses the right number of degrees of freedom (Shen et al., 2015).

Surface wave dispersion is fit quite well in the joint inversion. For 78% of the stations, the RMS misfit of the surface wave dispersion data for the average accepted model is less than 1. The average RMS misfit at all stations is 0.84 for the dispersion data.

There are nine stations in which RFs indicate that there is at least one discontinuity between the base of the sediments and the Moho or in the mantle, so that the smooth parameterization that we impose cannot fit the RF well. We discard the RF data for these nine stations. For the remaining RF data, the RMS misfit for the average accepted model is 1.0 on average. 88% of the stations have RMS misfit less than 1.5. The remaining stations with relatively large RF misfit are located mainly in the sedimentary basins.

For six stations, the RMS misfit of H/V measurements is larger than 2.5, while the RF and surface wave dispersion can be fit well. The reason may be that the H/V ratio is also sensitive to the V_P/V_S ratio and density of the shallow structure (Lin et al., 2012). For these stations we use the joint inversion of RF and surface wave dispersion only. The RMS misfit of the H/V ratio data for the average accepted model is 1.1 on average. 79% of the stations have RMS misfit less than 1.5. The misfit level is generally smaller than that in the USArray (Lin et al., 2012; Lin et al., 2014).

Data fit can be seen explicitly in Figure 3 for receiver functions, H/V and Rayleigh wave group and phase speeds for two stations: NE53 and NE8C. In each case predicted data are presented along with the data as solid lines, demonstrating how data are fit, on average. An example of poor fit to the H/V ratio is seen for station NE8C in the Songlaio Basin. All of the other data at these two stations are fit quite well.

3.4 Improvement in the 3-D model Compared with the Surface Wave Inversion

While surface wave dispersion data primarily constrain the velocity structure between interfaces (e.g., Shen et al., 2015), receiver functions (RFs) are sensitive to velocity contrasts. The H/V ratio further constrains upper crustal structure and thus mitigates artifacts spreading into deeper velocity structures (Lin et al., 2012).

The assimilation of the H/V ratio and especially the RF data has greatly improved the acc uracy of the estimate of the depths to discontinuities and *S*-wave speeds near them.

Figure 7 shows examples (at station NE53 in the Greater Xing'an Range) of prior and posterior distributions for several variables (sediment thickness, crustal thickness, Vs at 30 km depth in the crust, Vs at 80 km depth in the uppermost mantle) from the inversion based on surface wave dispersion alone (Fig. 2a - 2d) and all the three datasets (Fig. 2e - 2h). In each panel, the prior distribution is presented as the white histogram and the posterior distribution as the red histogram. The distributions of the depth of discontinuities (i.e. sediment thickness and crustal thickness) are broad in the surface wave dispersion inversion. In contrast, in the joint inversion, sedimentary and crustal thicknesses are much more tightly constrained. For station NE53, uncertainty in crustal thickness reduces from 4.97 km using surface wave dispersion data to 1.58 km in the joint inversion and the mean value reduces by approximately 2 km. In contrast, the effects of introducing RFs and H/V in the joint inversion are more subtle on Vs at 30 km and 80 km. At 30 km depth there is narrowing of the posterior distribution with a reduction of the standard deviation from 50 to 30 m/s. This happens because the RFs ensure that this point lies in the middle crust, not in the lower crust or the mantle.

The posterior distribution is displayed in a different way in Figure 8 for the joint inversion at two stations: NE53 and NE8C. In the depth functions, the grey profiles present the full width of the posterior distribution at each depth whereas the red lines show the one standard deviation profiles. The models beneath these two points, the former in the Greater Xing'an Range and the latter in the Songliao Basin, are quite different from each other. The station in the Songliao Basin has about 2 km of sediments and a mean crustal thickness of about 32.6 km whereas the crust is much thicker beneath the Greater Xing'an Range: 39.5 km.

The contrast between the average velocity structure of the shallow crust (top 4 km, including sediments) based on surface wave data alone and in the joint inversion is shown in Figure 9a,c. In the joint inversion, the structures imaged are sharper laterally and the low velocity anomaly in the center of the Songliao Basin is slower. Low velocities associated with the Erlian and Sanjian basins also appear. Perhaps more significantly, however, uncertainties are reduced strongly in the joint inversion as a comparison between Figures 9b and 9d illustrates. The Vs uncertainties for the uppermost crust are large when using surface wave dispersion alone (~0.17 km/s on average), especially beneath sedimentary basins, and reduce to ~0.11 km/s in the joint inversion.

Crustal thicknesses from the joint inversion (Fig. 9e) are also sharper and the variations more tightly confined between geological boundaries than in the inversion from surface wave dispersion alone (Fig. 9g). Notably, very thin crust is found to rim the eastern edge of the Songliao Basin and thicker crust is confined within the Jiamusi Massif east of the Jiayin-Mudanjiang Suture. The crust is also found to be somewhat thinner beneath the Greater Xing'an Range in the joint inversion. Uncertainties in crustal thickness average about 2.8 km in the joint inversion compared to about 4.4 km in the inversion of surface wave dispersion alone. Regions of continued high uncertainty in crustal thickness in the joint inversion include parts of the Songliao Basin, where the Moho *Ps* signals are obscured by sedimentary reverberations, and the Jiamusi Massif and near the Changbai Mountain Range, where there is a weak Moho *Ps* signal which we interpret as a gradient Moho caused perhaps by Moho complexity.

4. Results and Discussion

After inversion is performed at all stations, we interpolate the Vs models onto a 0.5°×0.5° regular grid using simple kriging interpolation (Schultz et al., 1998) at each depth guided by the estimated uncertainties.

4.1 Description and Discussion of the 3D Model

For the uppermost crust, a clear correlation is observed between Vs structure and near surface geological features (Fig. 9a). Basin areas, such as the Songliao, Erlian, and Sanjiang basins, are clearly delineated by low Vs anomalies. The slowest Vs anomalies of ~ 2 km/s are observed in the northern Songliao Basin, nearer to its western margin than the eastern margin. This is consistent with the evolution of the basin in the Cretaceous

Period, in which the eastern Songliao Basin was uplifted such that its depocentres migrated westward (Wang et al., 2007; Feng et al., 2010). A low Vs anomaly of ~2.5 km/s is also resolved in the Southwest Songliao Basin, which is related to the Kailu depression (Feng et al., 2010; Guo et al., 2014). Also, sediments are much thicker in the northern Songliao Basin in our model, which may be explained by larger postrift subsidence of the northern Songliao Basin than the southern part (Feng et al., 2010; Wei et al., 2010).

Shear wave speeds in the middle and lower crust show similar patterns of spatial variation (Fig.10b,c). Clear low Vs anomalies in the middle-to-lower crust are mainly observed beneath the Greater Xing'an Range (especially the southwestern and northeastern parts), the eastern margin of the Songliao Basin and in the wedge formed by the Yilan-Yitong and Dunhua-Mishan faults west of the Jiayin-Mudanjiang Suture. The slow anomalies beneath the Greater Xing'an Range are adjacent to the locations of two Pleistocene volcano groups marked in Figure 1a, which we refer to as the North/South Greater Xing'an Range Pleistocene Volcanic Zones. Slow anomalies beneath the eastern margin of the Songliao Basin extend southward toward the western Changbai Mountain Range are located in a region we refer to as the Northeast China Lineated Quaternary Volcanic Zone (Fig. 1a). The slow mid-crustal velocities beneath the Greater Xing'an Range may be due to granitic intrusions during the Mesozoic Era (Wu et al, 2003a; Wu et al 2003b). Beneath the Songliao Basin the high Vs anomalies (which appear more prominently in the lower than middle crust) may reflect a more mafic composition associated with rifting during basin formation in the late Mesozoic (Zhang et al., 2011). The fast anomaly observed beneath the Jiamusi Massif, bounded by the Jiayin-Mudanjiang suture to the west, may either indicate old basement which has been transported to its current location by block tectonic processes or perhaps magmatic underplating. Alternately, this fast anomaly could represent contamination of crustal velocity estimates with mantle velocities because crustal thickness is not well determined in this area (Fig. 9f).

Crustal thickness varies strongly across the region of study, thinning from ~45 km in the Greater Xing'an Range to ~30 km beneath the eastern Songliao Basin in the center of our study area (Fig. 9e). The most prominent anomaly is that Moho is uplifted about 6 km from west to east within the Songliao Basin, which agrees in general with estimates by

Tao et al. (2014). The thinnest crust near the eastern margin of the Songliao Basin lies within the Northeast China Lineated Quaternary Volcanic Zone. Several hypotheses could explain the eastward thinning of the crust in the Songliao Basin. First, the crust may have been thinned by stretching, and volcanoes penetrated the region opportunistically. Alternately, the thinner crust may have been created actively by long standing episodic volcanism that initiated in the Cenozoic and migrated flankward (Liu et al., 2001; Chen et al., 2007; Tao et al., 2014). Or, the topography on Moho could he interpreted as a westward tilt caused by a change in the direction of Pacific subduction toward the west in the late Cretaceous (Stepashko, 2006; Feng et al., 2010). This interpretation is consistent with the westward migration of the sedimentary depocentres.

Relatively thick crust of ~40 km is observed beneath the Jiamusi Massif near the eastward end of our study region. However, the crustal thickness uncertainties beneath the Jiamusi Massif are large (Fig. 9f) because receiver function data show weak or complicated Moho *Ps* signals in this area.The Vs jump (Fig. 10a) across the Moho (~0.6 km/s) is large beneath the Greater Xing'an range and reduces somewhat beneath the Songliao Basin.

Across most of the study area we observe at least a thin lithospheric lid right below the Moho. This can be seen most clearly in the vertical transects presented in Figures 12-15. The lid is largely imposed by the receiver functions, which constrain the jump in Vs across the Moho.

The strongest low velocity anomalies in the uppermost mantle are observed near the most active volcano in the region, Changbaishan Volcano, and generally east of the Yilan-Yitong Fault near the periphery of the study region (Fig. 10d,e,f and transects V1, V5, V6, Figs. 12, 15). During the Cenozoic Era, including in the Holocene, volcanic eruptions in Northeast China migrated eastward south of the Yilan-Yitong Fault (Liu et al., 2001; Chen et al., 2007). Vertical transects V1-V3, V4, and V5 all show this mantle low velocity anomaly east of the Songliao Basin. Lowest velocities are associated with the Changbai Mountain Range and are best seen in transects V1, V5 and V6. Tang et al. (2014) would interpret the low velocities found in the mantle beneath this part of our model as originating from subduction-induced upwelling that ascends through a gap in the subducting slab.

Lying beneath a thin mantle lid extending below the Songliao Basin, there are low velocity anomalies shown in transects V1-V3 and V5. On average, the upper mantle beneath the eastern Songliao Basin is slower than the western Songliao Basin, as shown clearly by transects V2 and V3 in Figures 13 and 14, consistent with the model of Tang et al. (2014). This is presumably because of proximity to the Northeast China Lineated Quaternary Volcanic Zone, which is arrayed nearer to the eastern margin of the basin. The lowest velocity anomaly extends from about 60 to 100 km depth beneath the Songliao Basin, and appears strongest in transect V2. The vertically arrayed fast, slow, fast pattern of anomalies beneath the Songliao Basin requires further investigation, particularly addressing whether it may provide evidence for recent delamination or the onset of lithospheric instabilities in the region. Alternately, the feature may reflect the crystal preferred orientation of anisotropic mantle minerals causing radial anisotropy that we are unable to resolve due to the lack of Love wave measurements. In contrast with the eastern parts of the basin, the mantle beneath the western Songliao Basin is generally fast and the lithosphere is thick (Transects V1, V2, V3, V5). Whatever is the cause of the mantle low velocities in the eastern basin, either advection of heat from the east or perhaps delamination, the phenomenon probably does not extend uniformly across the basin to the Greater Xing'an Range.

Slow anomalies in the mantle are also identified beneath the northern and southern Greater Xing'an Range (Fig. 10d,e,f), which appear more clearly in the vertical transects V1 and V4 in Figures 12 and 15, respectively, near to the locations of the Northern/Southern Greater Xing'an Range Pleistocene Volcanic Zones (Fig. 1a). In contrast, the central Greater Xing'an Range has high Vs anomalies in the upper mantle (Transects V3, V4) characteristic of thick lithosphere in this part of the mountain range. Thus, the mantle beneath the Greater Xing'an Range is inhomogeneous; only the northern and southern regions display mantle low velocities, which we interpret as thin lithosphere. The thin lithosphere beneath the southern and northern Greater Xing'an

Range may be consistent with hypothesized previous episodes of delamination in the Mesozoic Era (Wang et al., 2006; Zhang et al., 2010) with later Cenozoic volcanism occurring only where thin lithosphere is present (Figs. 1a, 15a).

4.2. Model Uncertainties

Figure 16a presents the spatial average of all the mean models and their associated 1σ uncertainties at each depth. To compute the spatial average of the mean and standard deviation we first stretch or thin the crustal and mantle parts of our model to the average crustal thickness across the study area. We then average the deformed profiles. This procedure prohibits averaging crustal velocities with mantle velocities at different locations due to Moho topography.

On average, the Moho depth from the surface (identified as black dashed line) is ~37.8 km in the study area. The average crustal velocity increases from ~3 km/sec near the surface to ~ 4.1 km/sec right above the Moho, while in the mantle it declines from ~4.45 km/sec right below Moho to ~4.35 km/sec at 150 km. Beneath Northeast China, the uppermost mantle velocities are ~2% slower than the global average (~4.5 km/sec from AK135), which may be attributed to the relatively high mantle temperatures associated with the volcanism in this area. The spatially averaged uncertainty (Fig. 16b) is the highest (0.1-0.25 km/sec) near the surface, due to the trade-off between the uppermost crustal velocity with sedimentary thickness. Within the crust, uncertainty is considerably smaller (<0.05 km/sec) but increases again in the lowermost crust. Between ~30 and ~50 km depth, the uncertainty peaks near Moho because the velocity-depth trade-off cannot be fully resolved everywhere in the study region. In the uppermost mantle, uncertainty is greater than in the crust (~0.08 km/sec), and it increases rapidly at depths greater than 100 km. The uncertainty shown here does not include bias (e.g., the possibly inaccurate Vp/Vs relationship or Q model used in the inversion) or covariances between depths.

4.3 Comparison of our Mantle Model with the Body Wave Model of Tang et al. (2014)

Tang et al. (2014) present a teleseismic *S*-wave tomography model across our study region, also based largely on data from the NECESS Array. Their model extends much deeper than ours and we present transects of this model to a depth of 300 km in Figures 12-14. We find that there are significant similarities between the two models in the lateral location of high and low velocities in the mantle, but greater there are dissimilarities concerning the distribution of the anomalies with depth. The lateral distribution of Vs anomalies, especially the outlines of sharp Vs contrasts display a high degree of consistency. A prominent high Vs anomaly, which bifurcates further north, is observed beneath the Greater Xing'an Range and the western flank of the Songliao Basin at depths greater than about 80 km in both models. In contrast, low Vs anomalies are shown near the Changbai Mountain Range, the Zhangguangcai Range and the Jiamusi massif. However, relatively weak low Vs anomalies beneath the southern Greater Xing'an Range, the Erlian Basin and the eastern flank of the Songliao Basin in our model are not clearly resolved in the body wave tomography. Moreover, the vertical distribution of Vs anomalies presents some discrepancies. For example, the slowest anomaly near the Changbai Mountain Range is located at ~110 km in our model, while it lies immediately below the Moho in Tang's model (Fig. 12). Perhaps the most notable difference between these two models is that a thin "high velocity lid" at the top of the mantle is present in our model. The assimilation of receiver functions in our inversion reduces the trade-off between Moho depth with lower crustal velocity and helps to better resolve such uppermost mantle structure (Shen et al., 2013a).

5. Conclusions

This study aims to refine the reference model China_2015 produced using surface wave dispersion data by Shen et al. (2015). We do this by assimilating the surface wave data in Northeast China used to construct China_2015 and introducing two new sets of measurements obtained using data from the NECESS array: receiver functions and Rayleigh wave H/V or ellipticity measurements. We document how the new data sets improve the vertical resolution of the resulting model within the crust, within the uppermost mantle, and between the crust and mantle and also improve the estimate of crustal thickness. Our 3D model is produced on a 0.5°x0.5° beneath the NECESS Array using a Bayesian Monte Carlo formalism in which the model and it uncertainties are determined from the mean and standard deviation of the posterior distribution of accepted models. A rich variety of structural features represented as shear wave speed anomalies are revealed in the final model. The model we present agrees well in the lateral distribution of fast and slow anomalies in the mantle with the teleseismic S-wave model produced by Tang et al. (2014), but there are differences in the vertical distribution of the imaged anomalies which are needed to fit the surface wave and receiver function data. In particular, we see a mantle lid beneath most of the study area and an enigmatic vertically arrayed "fast-slow-fast" anomaly underlying the Songliao Basin at depths between 60 km and 100 km that deserves further investigation. This feature could be thermal in origin, caused by westward advective heating from the Lineated Volcanic Zone to the east or possibly by the onset of a top-down lithospheric instability or delamination. Alternately, the feature may reflect the crystal preferred orientation of anisotropic mantle minerals causing radial anisotropy that we are unable to resolve due to the absence of Love wave measurements.

The principal scientific motivation for this study is to investigate the expression of intracontinental volcanism in the crust and uppermost mantle beneath Northeast China. Beneath what we call the Northeast China Lineated Quaternary Volcanic Zone (Fig. 1a), we find the thinnest crust in the region as well as slow mid-crustal velocities. Low mantle shear wave speeds, however, principally underlie the southern part of this volcanic zone near Changbaishan Volcano, but do extend westward beneath much of the eastern Songliao Basin and appears as thin lithosphere. In contrast, the Northern and Southern

Greater Xing'an Volcanic Zones (our terminology, Fig. 1a) display low velocity anomalies in both the crust and uppermost mantle but not crustal thinning. The central Greater Xing'an Range, which is well removed from Cenozoic volcanism, does not share the low mantle shear wave speeds found beneath the volcanic zones within the Greater Xing'an Range and the lithosphere is quite thick. The thin lithosphere beneath the Southern and Northern Greater Xing'an Range may coincide with the hypothesized previous episodes of delamination in the Mesozoic Era (Wang et al., 2006; Zhang et al., 2010) with later Cenozoic volcanism occurring only where thin lithosphere is present.

In the future, it would be beneficial to introduce Love waves in the analysis in order to investigate radial anisotropy in the crust and uppermost mantle. This may illuminate the so called fast-slow-fast mantle anomaly lying beneath the Songliao Basin, as this anomaly may result from the crystal preferred orientation of anisotropic minerals in the mantle. In addition, the strong similarity between the lateral distribution of depth-integrated velocity anomalies in the mantle between our model and the body wave model of Tang et al. (2015) calls for the joint inversion of our data together with teleseismic body wave data as done, for example, using USArray data by Obrebski et al. (2011) and by West et al. (2004) using RISTRA project data.

Acknowledgments

DK and JN had extended work visits to the University of Colorado during which aspects of this work were completed, and they thank the Chinese Geological Survey (GZH201200504) for support. . We thank all the people who participated in the NECESS Array project for installing/dismantling and servicing the seismic array. Aspects of this research was supported by NSF grant EAR-1246925 at the University of Colorado at Boulder. The facilities of IRIS Data Services, and specifically the IRIS Data Management Center, were used for access to waveforms, related metadata, and/or derived products used in this study. IRIS Data Services are funded through the Seismological Facilities for the Advancement of Geoscience and EarthScope (SAGE) Proposal of the National Science Foundation under Cooperative Agreement EAR-1261681. This work utilized the Janus supercomputer, which is supported by the National Science Foundation (award number CNS-0821794), the University of Colorado at Boulder, the University of Colorado Denver and the National Center for Atmospheric Research. The Janus supercomputer is operated by the University of Colorado at Boulder.

References

Bao, X., Song, X., & Li, J., 2015. High-resolution lithospheric structure beneath Mainland China from ambient noise and earthquake surface-wave tomography, *Earth and Planetary Science Letters*, 417, 132-141.

Barmin, M.P., M.H. Ritzwoller, and A.L. Levshin, 2001. A fast and reliable method for surface wave tomography, *Pure Appl. Geophys.*, 158(8), 1351 – 1375.

Bensen, G.D., Ritzwoller, M.H., Barmin, M.P., Levshin, A.L., Lin, F., Moschetti, M.P., Shapiro, N.M. & Yang, Y., 2007. Processing seismic ambient noise data to obtain reliable broad-band surface wave dispersion measurements, *Geophys. J. Int.*, 169, 1239–1260.

Bodin, T., Sambridge, M., Tkalčić, H., Arroucau, P., Gallagher, K. & Rawlinson, N., 2012. Transdimensional inversion of receiver functions and surface wave dispersion, *J. Geophys. Res.*, 117, B02301, doi:10.1029/2011JB008560.

Boore, D. M., & Toksöz, M. N., 1969. Rayleigh wave particle motion and crustal structure. *Bulletin of the seismological Society of America*, 59(1), 331-346.

Brocher, T. M., 2005. Empirical relations between elastic wavespeeds and density in the Earth's crust. *Bull. Seismol. Soc. Am.*, 95(6), 2081-2092.

Chen, Z., Liu, G., Huang, Z., Lu, X., Luo, Q., Ding, X., 2014. Controls of oil family distribution and composition in nonmarine petroleum systems: A case study from Inner Mongolia Erlian basin, Northern China. *J. Asian Earth Sci*. 10/2014; 92:36–52. DOI: 10.1016/j.jseaes.2014.06.006

Chen, Y., Zhang, Y., Graham, D., Su, S., Deng, J., 2007. Geochemistry of Cenozoic basalts and mantle xenoliths in Northeast China. *Lithos* 96 (1–2), 108–126.

Dalton, C.A. & Ekstrom, G., 2006. Global models of surface wave attenuation, *J. geophys. Res.*, 111(B10), 5317, doi:10.1029/2005JB003.

Feng, Z.Q., Jia, C.Z., Xie, X.N., Zhang, S., Feng, Z.H., Timothy, A.C., 2010. Tectonostratigraphic units and stratigraphic sequences of the nonmarine Songliao basin, northeast China. *Basin Research*, 22, 79–95.

Guo, Z., Y. J. Chen, J. Ning, Y. Feng, S. P. Grand, F. Niu, H. Kawakatsu, S. Tanaka, M. Obayashi, and J. Ni (2015), High resolution 3-D crustal structure beneath NE China from joint inversion of ambient noise and receiver functions using NECESSArray data, *Earth and Planetary Science Letters*, 416, 1–11, doi:10.1016/j.epsl.2015.01.044.

Hacker, B.R. and G.A. Abers, 2004. Subduction Factory 3: An Excel worksheet and macro for calculating the densities, seismic wave speeds, and H2O contents of minerals and rocks at pressure and temperature. *Geochem. Geophys. Geodyn*. 5, Q01005, doi:10.1029/2003GC000614.

Huang, Z., Su, W., Peng, Y., Zheng, Y., & Li, H., 2003. Rayleigh wave tomography of China and adjacent regions. *Journal of Geophysical Research: Solid Earth* (1978–2012), 108(B2).

Julià J., Ammon, C.J., Herrmann, R.B., Correig, A.M., 2000. Joint inversion of receiver function and surface wave dispersion observations. *Geophys. J. Int,* 143, 99-112.

Kanamori, H., & Anderson, D. L., 1977. Importance of physical dispersion in surface wave and free oscillation problems: Review. *Reviews of Geophysic*s,15(1), 105-112.

Kennett B.L.N., Engdahl E.R. & Buland R.,1995. Constraints on seismic velocities in the earth from travel times. *Geophys. J. Int*, 122, 108-124

Li, Y., Wu, Q., Pan, J., & Sun, L., 2012. S-wave velocity structure of northeastern China from joint inversion of Rayleigh wave phase and group velocities. *Geophys. J. Int.,* 190(1), 105-115.

Li, Y., Wu, Q., Pan, J., Zhang, F., & Yu, D., 2013. An upper-mantle S-wave velocity model for East Asia from Rayleigh wave tomography. *Earth and Planetary Science Letters*, 377, 367-377.

Ligorria J. P. and Ammon C. J., 1999. Iterative deconvolution and receiver-function estimation. *Bull. Seism. Soc. Am.*, 89, 1395–400

Lin, F.C., Schmandt, B. & Tsai, V.C., 2012. Joint inversion of Rayleigh wave phase velocity and ellipticity using USArray: constraining velocity and density structure in the upper crust, *Geophys. Res. Lett.*, 39(L12303), doi:10.1029/2012GL052196.

Lin, F.C., V.C. Tsai, and B. Schmandt, 2014. 3-D crustal structure of the western United States: application of Rayleigh-wave ellipticity extracted from noise cross-correlations, *Geophys. J. Int*, doi: 10.1093/gji/ggu160.

Lin, F.C. & Ritzwoller, M.H., 2011. Helmholtz surface wave tomography for isotropic and azimuthally anisotropic structure, *Geophys. J. Int.*, 186, 1104–1120.

Lin, F.C., Ritzwoller, M.H. & Snieder, R., 2009. Eikonal tomography: surface wave tomography by phase front tracking across a regional broadband seismic array, *Geophys. J. Int.*, 177, 1091–1110.

Lin, Q., Ge, W. C., Sun, D. Y., Wu, F. Y., Chong, K. W., Kyung, D. M., ... & Sung, H. Y.,1998. Tectonic significance of Mesozoic volcanic rocks in northeastern China. *Scientia Geologica Sinica*, 33(2), 129-138.

Liu, J.Q., Han, J.T., Fyfe, W.S., 2001. Cenozoic episodic volcanism and continental rifting in northeast China and possible link to Japan Sea development as revealed from K–Ar geochronology. *Tectonophysics* 339, 385–401.

Mosegaard, K., & Tarantola, A., 1995. Monte Carlo sampling of solutions to inverse problems. *Journal of Geophysical Research: Solid Earth* (1978–2012),100(B7), 12431-12447.

Niu, F., Li, J., 2011. Component azimuths of the CEArray stations estimated from P-wave particle motion. *Earthquake Science*, 24(1), 3-13.

Obrebski, M., Allen, R. M., Pollitz, F., & Hung, S. H., 2011. Lithosphere–asthenosphere interaction beneath the western United States from the joint inversion of body-wave traveltimes and surface-wave phase velocities.*Geophysical Journal International*, 185(2), 1003-1021.

Obrebski, M., Allen, R. M., Zhang, F., Pan, J., Wu, Q., and Hung, S. H., (2012). Shear wave tomography of China using joint inversion of body and surface wave constraints, *J. Geophys. Res.*, 117(B1), B01311, doi:10.1029/2011jb008349.

Ren, J., K. Tamaki, S. Li, and J. Zhang, 2002. Late Mesozoic and Cenozoic rifting and its dynamic setting in eastern China and adjacent areas: *Tectonophysic*s, v. 344, p.

175–205, doi:10.1016/S0040-1951(01)00271-2.

Schultz, C. A, S. C. Myers, J Hipp, and C. J. Young, 1998. Non-stationary Bayesian kriging: A predictive technique to generate spatial corrections for seismic detection, location and identification, *Bull. Seism. Soc. Am.*, 88, 1275–1288.

Shen, W., M.H. Ritzwoller, D. Kang, Y. Kim, J. Ning, F.-C. Lin, W. Wang, Y. Zheng, and L. Zhou, 2015. A seismic reference model for the crust and uppermost mantle beneath China from surface wave dispersion, *Geophys. J. Int*., submitted.

Shen, W., Ritzwoller, M.H., Schulte-Pelkum, V., Lin, F.-C., 2013a. Joint inversion of surface wave dispersion and receiver functions: a Bayesian Monte-Carlo approach. *Geophys. J. Int.*, 192(2), 807-836.

Shen, W., Ritzwoller, M.H., Schulte-Pelkum, V., 2013b. A 3-D model of the crust and uppermost mantle beneath the Central and Western US by joint inversion of receiver functions and surface wave dispersion. *Journal of Geophysical Research - Solid Earth*, 118(1), 262-276.

Stepashko, A.A., 2006. The Cretaceous dynamics of the Pacific plate and stages of magmatic activity in Northeastern Asia. *Geotectonics,* 40 (3), 225–235.

Tang, Y., Obayashi, M., Niu, F., Grand, S.P., Chen, Y.J., Kawakatsu, H., Tanaka, S., Ning, J., Ni, J.F., 2014. Changbaishan volcanism in northeast China linked to subduction induced mantle upwelling. *Nat. Geosci.* 7, 470–475.

Tanimoto, T., and L. Rivera, 2008. The ZH ratio method for long-period seismic data: Sensitivity kernels and observational techniques, *Geophys. J. Int*., 172, 187–198, doi:10.1111/j.1365-246X.2007.03609.x.

Tao, K., Niu, F., Ning, J., Chen, Y.J., Grand, S., Kawakatsu, H., Tanaka, S., Obayashi, M., Ni, J., 2014. Crustal structure beneath NE China imaged by NECESSArray receiver function data. *Earth and Planetary Science Letters,* 398, 48–57.

Wang, F., Zhou, X. H., Zhang, L. C., Ying, J. F., Zhang, Y. T., Wu, F. Y., & Zhu, R. X., 2006. Late Mesozoic volcanism in the Great Xing'an Range (NE China): timing and implications for the dynamic setting of NE Asia. *Earth and Planetary Science Letters*, 251(1), 179-198.

Wang, P. J., X. Xie, F. Mattern, Y. Ren, D. Zhu, and X. Sun (2007). The Cretaceous Songliao Basin: Volcanogenic succession, sedimentary sequence and tectonic evolution, NE China, *Acta Geol. Sin.*, 81, 1002–1011.

Watson, M.P., Hayward, A.B., Parkinson, D.N., Zhang, Z.M., 1987. Plate tectonic history, basin development and petroleum source rock deposition onshore China. *Mar. Pet. Geol*. 4, 205–225.

Wei, H. H., Liu, J. L., & Meng, Q. R., 2010. Structural and sedimentary evolution of the southern Songliao Basin, northeast China, and implications for hydrocarbon prospectivity. *AAPG bulletin*, 94(4), 531-564.

West, M., Gao, W., & Grand, S., 2004. A simple approach to the joint inversion of seismic body and surface waves applied to the southwest US. *Geophysical research letters*, 31(15).

Wu, F., Jahn, B., Wilde, S.A., Lo, C., Yui, T., Lin, Q., Ge, W., Sun, D., 2003a. Highly fractionated I-type granites in NE China (I): geochronology and petrogenesis. *Lithos* 66 (3–4), 241–273.-

Wu, F., Jahn, B., Wilde, S.A., Lo, C., Yui, T., Lin, Q., Ge, W., Sun, D., 2003b. Highly fractionated I-type granites in NE China (II): isotopic geochemistry and implications for crustal growth in the Phanerozoic. *Lithos* 67 (3–4), 191–204

Wu, F.Y., Sun, D.Y., Ge, W.C., Zhang, Y.B., Grant, M.L., Wilde, S.A., Jahn, B.M., 2011. Geochronology of the Phanerozoic granitoids in northeastern China. *J. Asian Earth Sci*.41, 1–30.

Xie, J., M.H. Ritzwoller, S. Brownlee, and B. Hacker, 2015. Inferring the oriented elastic tensor from surface wave observations: Preliminary application across the Western US, *Geophys. J. Int.*, 201, 996-1021.

Yang, Y., et al., 2010. Rayleigh wave phase velocity maps of Tibet and the surrounding regions from ambient seismic noise tomography, *Geochem., Geophys., Geosys.*, 11(8), Q08010, doi:10.1029/2010GC003119.

Yang, Y., Ritzwoller, M.H., Zheng, Y., Shen, W., Levshin, A.L., Xie, Z., 2012. A synoptic view of the distribution and connectivity of the mid-crustal low velocity zone beneath Tibet. Journal of Geophysical Research - Solid Earth, 117(B4), B04303.

Yano, T., T. Tanimoto, and L. Rivera, 2009. The ZH ratio method for long-period seismic data: inversion for S-wave velocity structure, *Geophys. J. Int*., 179, 413–424, doi:10.1111/j.1365-246X.2009.04293.x.

Zhang, F-Q, Chen, H-L, Yang, S-F, 2012. Late Mesozoic-Cenozoic evolution of the

Sanjiang Basin in NE China and its tectonic implications for the West Pacific continental margin. *J. Asian Earth Sci.*, 49: pp. 287-299

Zhang, F.Q., Chen, H.L., Yu, X., Dong, C.W., Yang, S.F., Pang, Y.M., Batt, G.E., 2011.Early Cretaceous volcanism in the northern Songliao Basin, NE China, and its geodynamic implication. *Gondwana Res.* 19 (1), 163–176.

Zhang, J. H., Gao, S., Ge, W. C., Wu, F. Y., Yang, J. H., Wilde, S. A., & Li, M., 2010. Geochronology of the Mesozoic volcanic rocks in the Great Xing'an Range, northeastern China: implications for subduction-induced delamination. *Chemical Geology*, 276(3), 144-165.

Zheng, S., Sun, X., Song, X., Yang, Y., & Ritzwoller, M. H., 2008. Surface wave tomography of China from ambient seismic noise correlation.*Geochemistry, Geophysics, Geosystems*, 9(5).

Zheng, Y., W. Shen, L. Zhou, Y. Yang, Z. Xie, and M.H. Ritzwoller, 2011. Crust and uppermost mantle beneath the North China Craton, northeastern China, and the Sea of Japan from ambient noise tomography, *J. Geophys. Res.*, 116, B12312, doi:10.1029/2011JB008637

Zhou, L., J. Xie, W. Shen, Y. Zheng, Y. Yang. H. Shi, and M.H. Ritzwoller, 2012. The structure of the crust and uppermost mantle beneath South China from ambient noise and earthquake tomography, *Geophys. J. Int.*, doi: 10.1111/j.1365-246X.2012.05423.x.

Table 1. Model parameterization

Model parameters	Perturbation
Sedimentary layer thickness	±100%
Sedimentary layer Vsv	±1.5 km/s
Crystalline crustal thickness	±15 km
B-spline coefficients, crust	±20%
B-spline coefficients, mantle	±20%

Figure Captions

Figure 1. (a) Reference map of geological features, faults, and sedimentary basins, displaying the location and age of the principal volcanoes (From Chen et al., 2007). Sedimentary basins: ELB – Erlian Basin; HLB – Hailar Basin; SLB – Songliao Basin; SJB – Sanjiang Basin; KD – Kailu Depression. Mountain ranges: GXAR – Greater Xing'an Range; LXAR – Lesser Xing'an Range; ZGCR – Zhangguancai Range; CBM – Changbai Mountain Range. Faults/Sutures: S1 (yellow dashed line) – Jiayin-Mudanjiang Suture; F1 – Yilan-Yitong Fault; F2 – Dunhua-Mishan Fault. The Jiamusi Massif (not shown) lies east of the Jiayin-Mudanjiang Suture and includes the Sanjiang Basin. Blue ovals: Northern/Southern Greater Xing'an Range Pleistocene Volcanic Zones. Pink oval: Northeast China Lineated Quaternary Volcanic Zone. (b) Station map where symbol color identifies the data used in the inversion: DISP – Rayleigh wave group and phase speed; HV – Rayleigh wave H/V ratio; RF – receiver functions. Symbol type identifies where sediments are modeled with one (triangles) or two (squares) layers. Locations of vertical transects are identified as V1, …, V6, shown in Figs. 12-15. Stations NE53 and NE8C are identified.

Figure 2. Example maps of Rayleigh wave H/V ratio (or ellipticity) at (a) 24 sec and (c) 40 sec period. Associated uncertainties in H/V ratio are also presented in (b) and (d).

Figure 3. Examples of data used in the joint inversion for stations (Left Column) NE53 and (Right Column) NE8C, whose locations are identified in Fig. 1b. (a,b) Receiver functions with uncertainties shown as the grey envelopes, (c,d) Rayleigh wave H/V ratios where uncertainties are presented as one standard deviation error bars, and (e,f) Rayleigh wave group and phase speed curves with uncertainties presented as one standard deviation error bars. Solid lines in each panel are the predictions from the mean of the posterior distribution of model beneath each station, where for dispersion the red line is

phase speed and the blue line is group speed. RMS misfit for the mean of the posterior distribution is presented for each data type alone on each panel and for the joint inversion at top of each column.

Figure 4. Comparison between earthquake based tomographic maps for the 60 sec Rayleigh wave using (a) eikonal tomography and (b) Helmholtz tomography. (c) The difference between the two maps. (d) Histogram of the differences between the two maps: mean difference is 3 m/s, standard deviation of the difference is 16 m/s.

Figure 5. (a)-(d) Example Rayleigh wave phase speed maps determined from ambient noise tomography by Shen et al. (2015) at four periods: 10 sec, 20 sec, 30 sec, 40 sec. (e) Rayleigh wave speed map determined by Helmholtz (earthquake) tomography at 40 sec period to compare with the ambient noise result in (d). (e) Histogram of the difference between the 40 sec maps from ambient noise and earthquake tomography: mean difference is 4 m/s, standard deviation of the difference is 27 m/s.

Figure 6. (a) The quality controlled observed receiver functions are plotted along back-azimuth for station NE53 (location identified in Fig. 1b). (b) The estimated receiver functions, $H(\theta,t)$, from harmonic stripping. (c-e) The three estimated harmonic components from harmonic stripping. For most stations, the receiver function we use in the joint inversion here is the average of $H(\theta,t)$ between azimuths of 120° and 240°.

Figure 7. Examples of the prior and posterior distributions for several model variables at station NE53 (location identified in Fig. 1b), where the prior is shown with the white histogram and the posterior by the red histogram. The left column (a,c,e,g) is for the inversion based on surface wave dispersion alone and the right column (b,d,f,h) presents results from the joint inversion including receiver functions and H/V ratio. (a,b) Sedimentary thickness, in km. (c,d) Vs at 30 km depth in km/s. (e,f) Crustal thickness, in km. (g,h) Vs at 80 km, in km/s. The mean and standard deviation of both prior and

posterior distributions are labeled on each panel, where the standard deviation appears in parentheses.

Figure 8. Vertical envelopes (grey shaded regions) formed by the full set of accepted models in the posterior distribution at two stations (NE53, NE8C) whose locations are identified in Fig. 1b. The bold black lines identify the mean of each distribution (from which the solid curves in Fig. 3 are computed) and the red lines identify the one standard deviation perturbations in the posterior distribution at each depth.

Figure 9. Comparison between the estimated models and uncertainties from the inversion of surface wave dispersion alone (SW) and from the joint inversion (surface wave dispersion, receiver functions and H/V ratio, Joint). Maps of the mean of the posterior distribution of the average of Vs at depths from 0 to 4 km from (a) the joint inversion and (c) the surface wave dispersion. Uncertainties in the Vs averaged from 0-4 km are shown in (b) and (d), where uncertainty is one standard deviation from the mean of the posterior distribution. (e,g) Mean of the posterior distribution of crustal thickness from the joint and surface wave inversions, respectively. (f,h) Associated one standard deviation uncertainties in crustal thickness.

Figure 10. Maps of the mean of the posterior distribution at each location from the joint inversion for (a) the jump in Vs across the Moho (constrained to be positive), (b) Vs in the middle crust (averaged between $\pm$2km of the middle of the crystalline crust), (c) Vs in the lower crust (averaged from 4 km above Moho to Moho), (d) Vs at 60 km depth (averaged from 55 to 65 km), (e) Vs at 90 km depth (averaged from 80 to 100 km), and (f) Vs at 120 km depth (average from 110 to 130 km). Mantle velocities are defined as perturbations relative to 4.4 km/s (in percent) and crustal velocities are plotted in absolute terms, km/s.

Figure 11. Maps of one standard deviation relative to the mean of the posterior distribution from the joint inversion, interpreted as local uncertainty, where the means of

the corresponding variables have been plotted in Fig. 10.

Figure 12. (a) A vertical transect (V1, location shown in Fig. 1b) through our Vs model plotted to 150 km, compared with (b) Vs values from the body wave model of Tang et al. (2014) plotted to 300 km depth. Absolute velocities are presented in the crust (in km/s) and in the mantle perturbations are plotted relative to 4.4 km/s (in percent). Surface topography is indicated in each panel together with location names, defined in Fig. 1a. Nearby volcanoes are also indicated, color-coded by age as in Fig. 1a.

Figure 13. Similar to Fig. 12, but for vertical transect V2.

Figure 14. Similar to Fig. 12, but for vertical transect V3.

Figure 15. Three vertical transects (V4-V6, locations shown in Fig. 1b) through our Vs model plotted to 150 km with the same velocity scales as in Figs. 12-14.

Figure 16. (a) Average shear velocity profile across the study region. (b) Uncertainty as a function of depth averaged across the study region.

Figure1

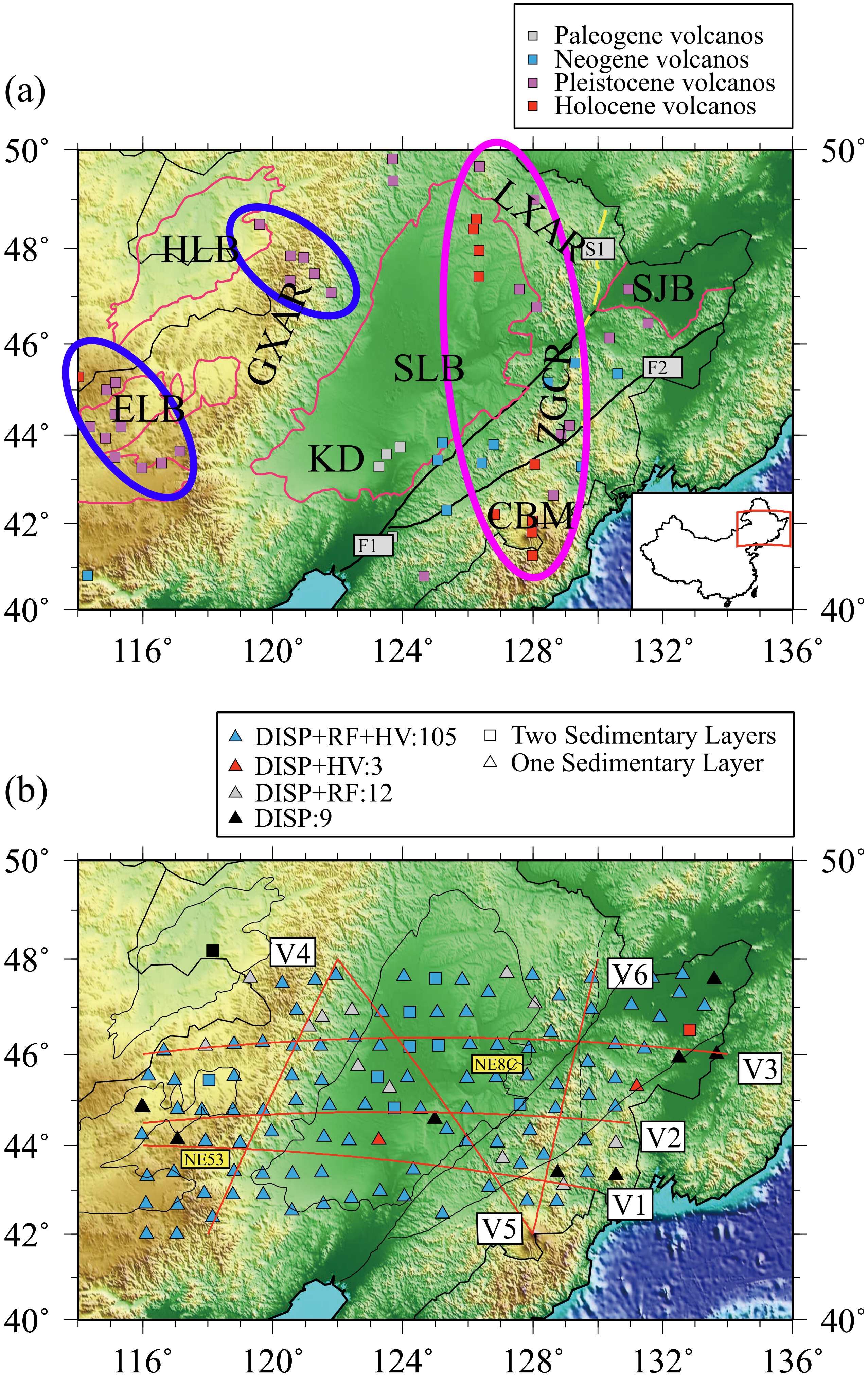
(a)
Paleogene volcanos
Neogene volcanos
Pleistocene volcanos
Holocene volcanos
HLB
GXAR
ELB
SLB
KD
LXAR
S1
SJB
ZGCR
F2
CBM
F1
50°
48°
46°
44°
42°
40°
116°
120°
124°
128°
132°
136°
(b)
DISP+RF+HV:105
DISP+HV:3
DISP+RF:12
DISP:9
Two Sedimentary Layers
One Sedimentary Layer
V4
V6
V3
V2
V1
V5
NE8C
NE53

Figure 2

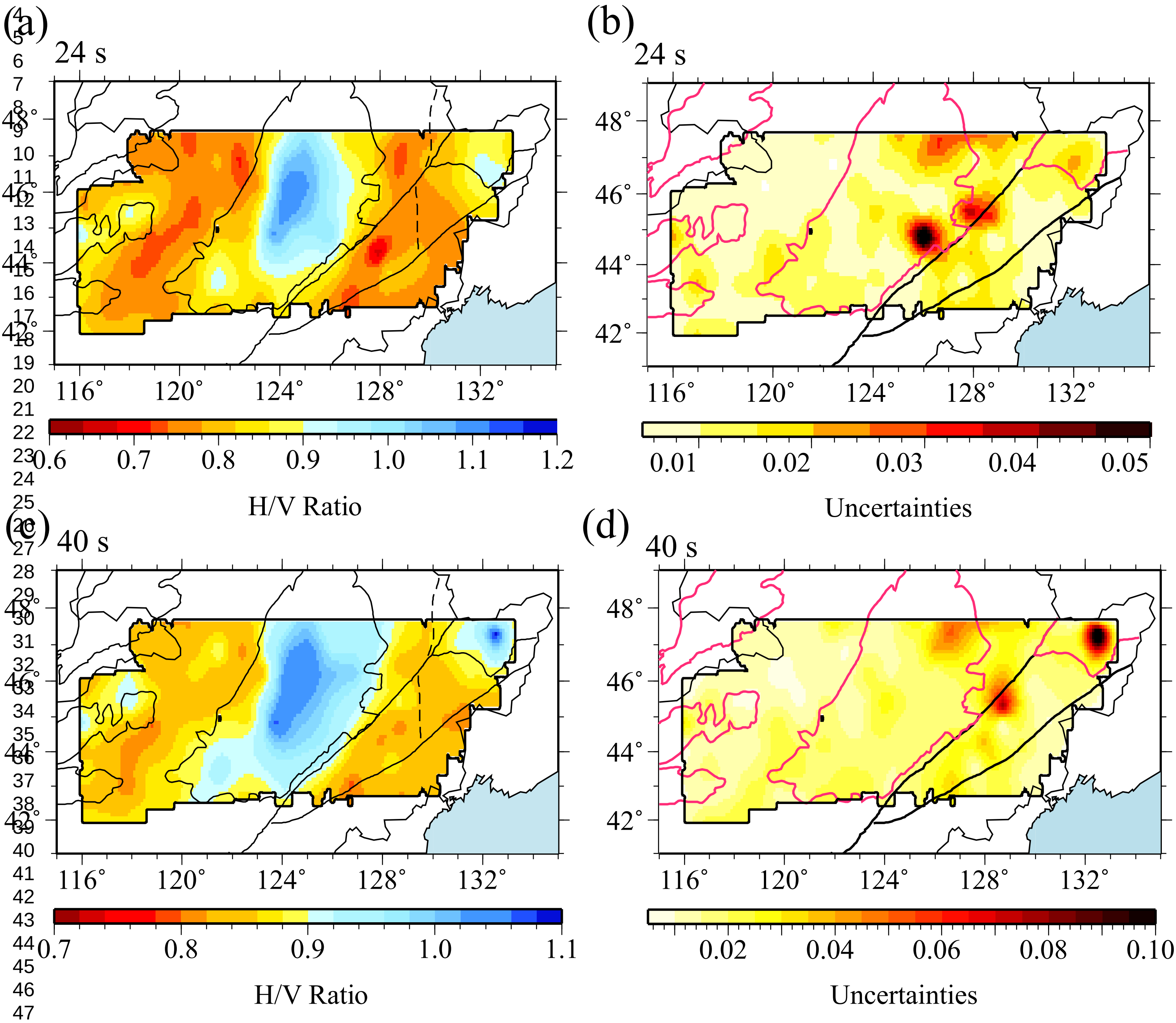
(a)
24 s
48°
46°
44°
42°
116°
120°
124°
128°
132°
0.6
0.7
0.8
0.9
1.0
1.1
1.2
H/V Ratio
(b)
24 s
48°
46°
44°
42°
116°
120°
124°
128°
132°
0.01
0.02
0.03
0.04
0.05
Uncertainties
(c)
40 s
48°
46°
44°
42°
116°
120°
124°
128°
132°
0.7
0.8
0.9
1.0
1.1
H/V Ratio
(d)
40 s
48°
46°
44°
42°
116°
120°
124°
128°
132°
0.02
0.04
0.06
0.08
0.10
Uncertainties

Figure 3

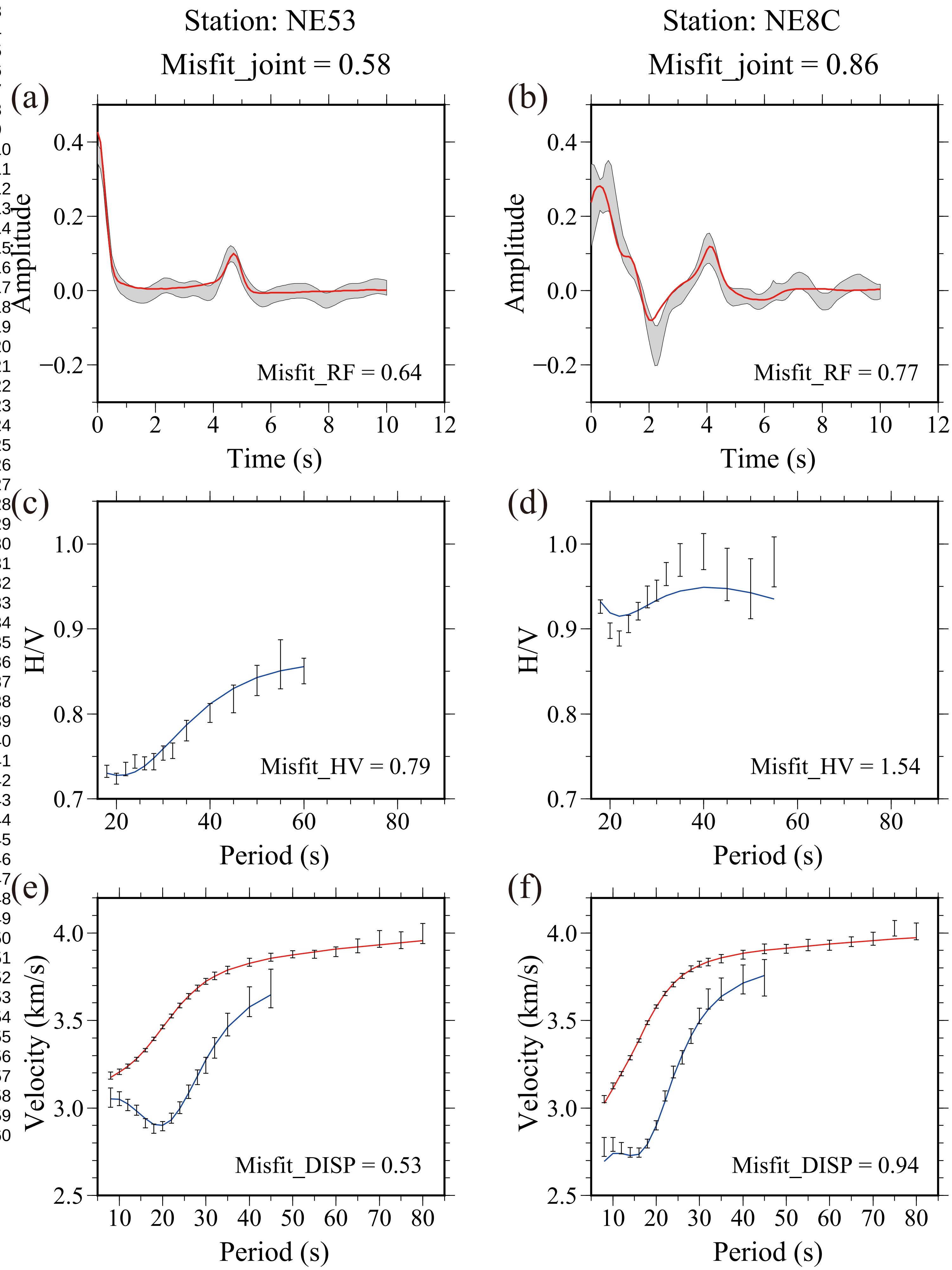
Station: NE53
Misfit_joint = 0.58
Station: NE8C
Misfit_joint = 0.86
(a)
(b)
Amplitude
Time (s)
Misfit_RF = 0.64
Misfit_RF = 0.77
(c)
(d)
H/V
Period (s)
Misfit_HV = 0.79
Misfit_HV = 1.54
(e)
(f)
Velocity (km/s)
Misfit_DISP = 0.53
Misfit_DISP = 0.94

Figure 4

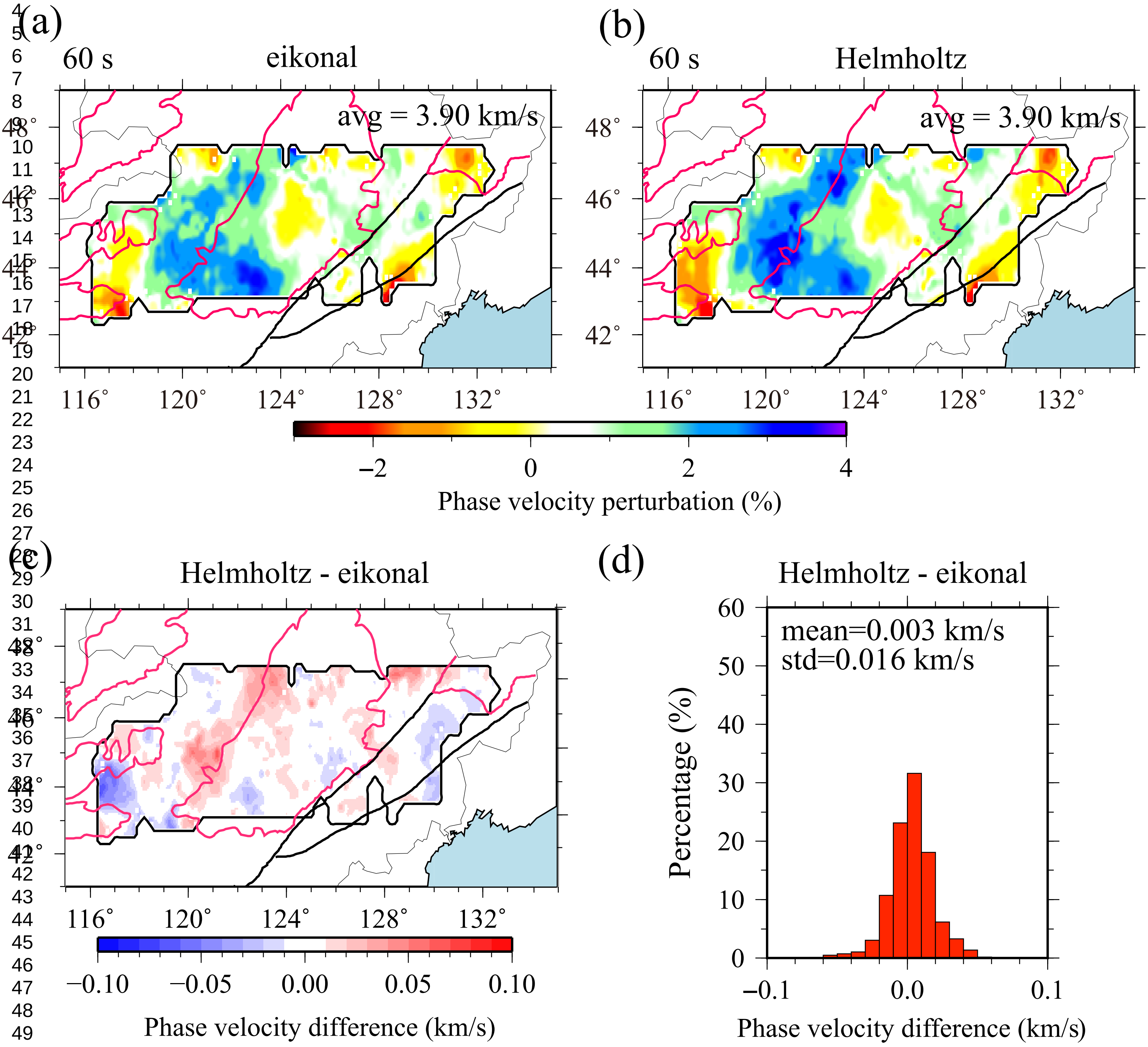

(a)
60 s
eikonal
avg = 3.90 km/s
(b)
60 s
Helmholtz
avg = 3.90 km/s
48°
46°
44°
42°
116°
120°
124°
128°
132°
−2
0
2
4
Phase velocity perturbation (%)
(c)
Helmholtz - eikonal
−0.10
−0.05
0.00
0.05
0.10
Phase velocity difference (km/s)
(d)
Helmholtz - eikonal
mean=0.003 km/s
std=0.016 km/s
Percentage (%)
0
10
20
30
40
50
60
−0.1
0.0
0.1
Phase velocity difference (km/s)

Figure 5

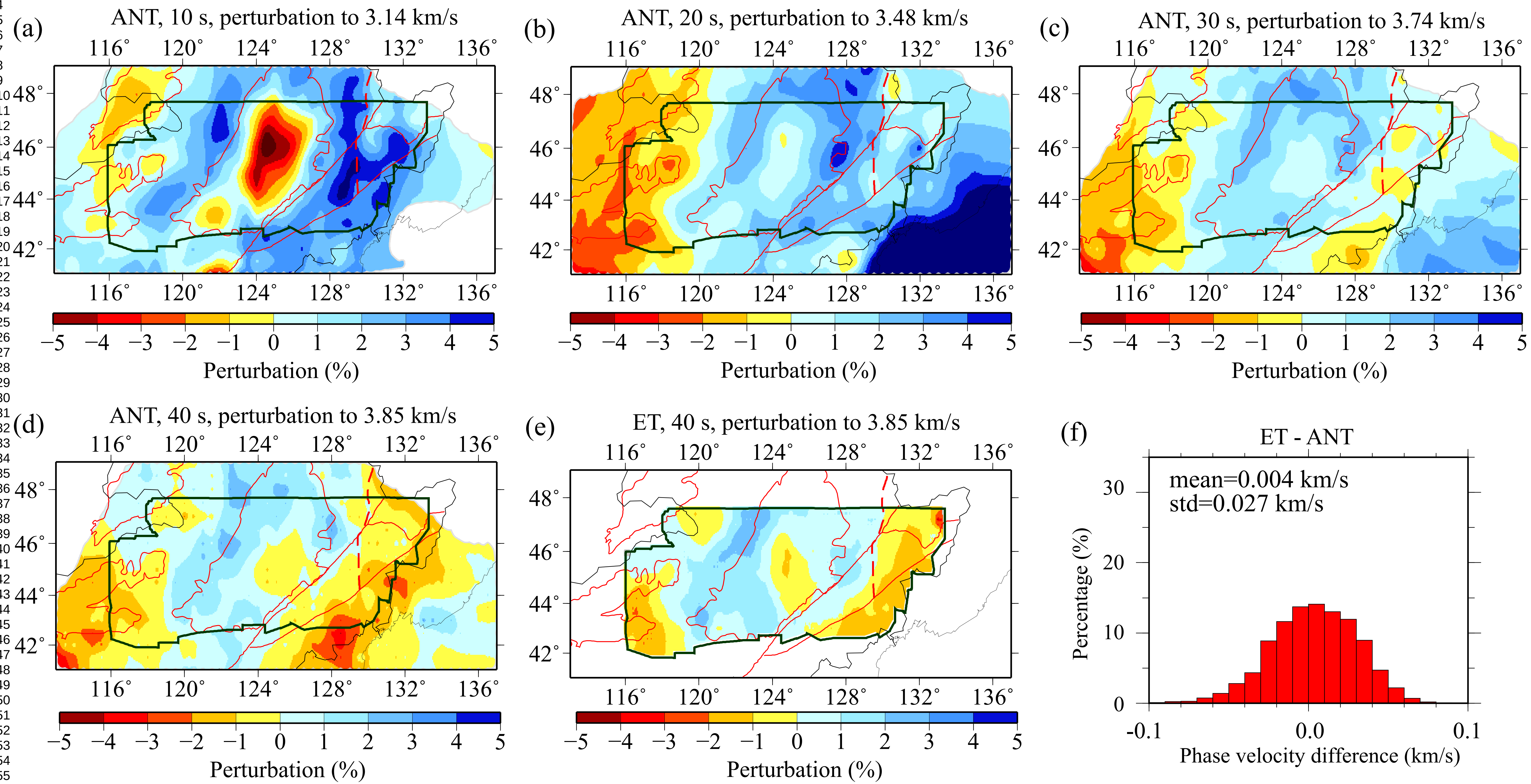
(a)
ANT, 10 s, perturbation to 3.14 km/s
(b)
ANT, 20 s, perturbation to 3.48 km/s
(c)
ANT, 30 s, perturbation to 3.74 km/s
(d)
ANT, 40 s, perturbation to 3.85 km/s
(e)
ET, 40 s, perturbation to 3.85 km/s
116° 120° 124° 128° 132° 136°
42° 44° 46° 48°
−5 −4 −3 −2 −1 0 1 2 3 4 5
Perturbation (%)
(f)
ET - ANT
mean=0.004 km/s
std=0.027 km/s
Percentage (%)
0 10 20 30
-0.1 0.0 0.1
Phase velocity difference (km/s)

Figure 6

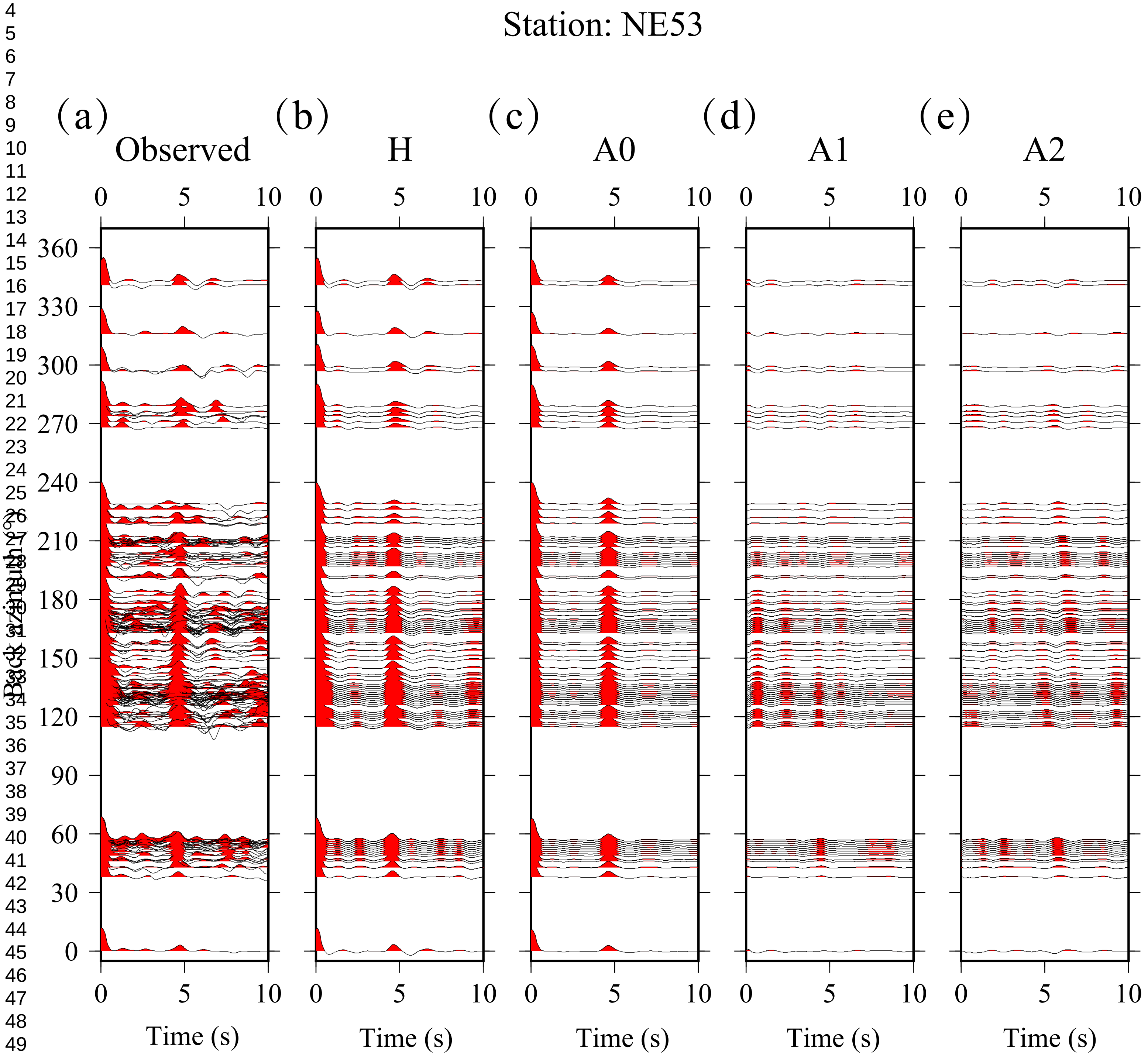
Station: NE53
(a) Observed
(b) H
(c) A0
(d) A1
(e) A2
0
5
10
360
330
300
270
240
210
180
150
120
90
60
30
0
Back azimuth (°)
Time (s)

Figure 7

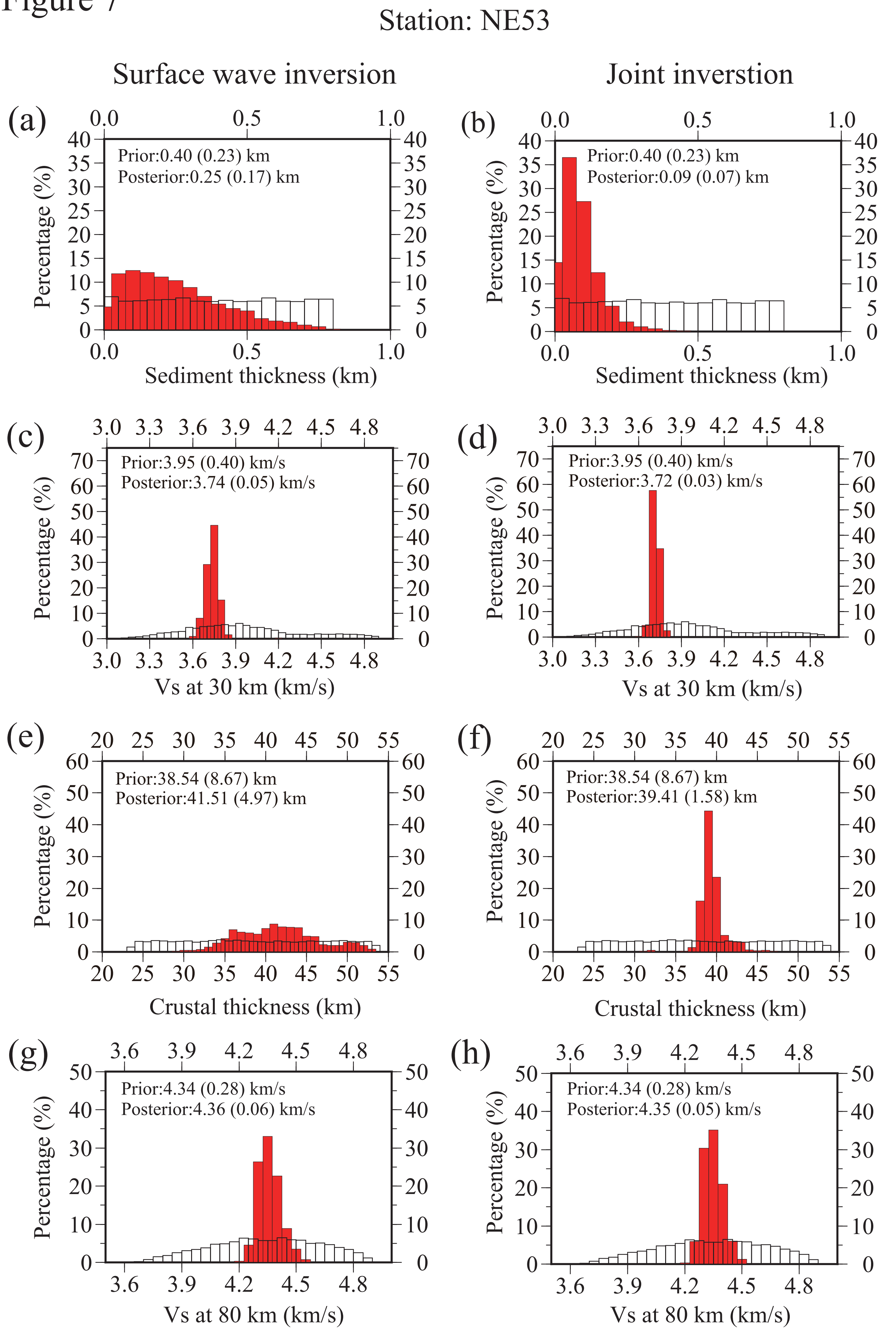
Station: NE53
Surface wave inversion
Joint inverstion
(a)
Prior:0.40 (0.23) km
Posterior:0.25 (0.17) km
Percentage (%)
Sediment thickness (km)
(b)
Prior:0.40 (0.23) km
Posterior:0.09 (0.07) km
Percentage (%)
Sediment thickness (km)
(c)
Prior:3.95 (0.40) km/s
Posterior:3.74 (0.05) km/s
Percentage (%)
Vs at 30 km (km/s)
(d)
Prior:3.95 (0.40) km/s
Posterior:3.72 (0.03) km/s
Percentage (%)
Vs at 30 km (km/s)
(e)
Prior:38.54 (8.67) km
Posterior:41.51 (4.97) km
Percentage (%)
Crustal thickness (km)
(f)
Prior:38.54 (8.67) km
Posterior:39.41 (1.58) km
Percentage (%)
Crustal thickness (km)
(g)
Prior:4.34 (0.28) km/s
Posterior:4.36 (0.06) km/s
Percentage (%)
Vs at 80 km (km/s)
(h)
Prior:4.34 (0.28) km/s
Posterior:4.35 (0.05) km/s
Percentage (%)
Vs at 80 km (km/s)

Figure 8

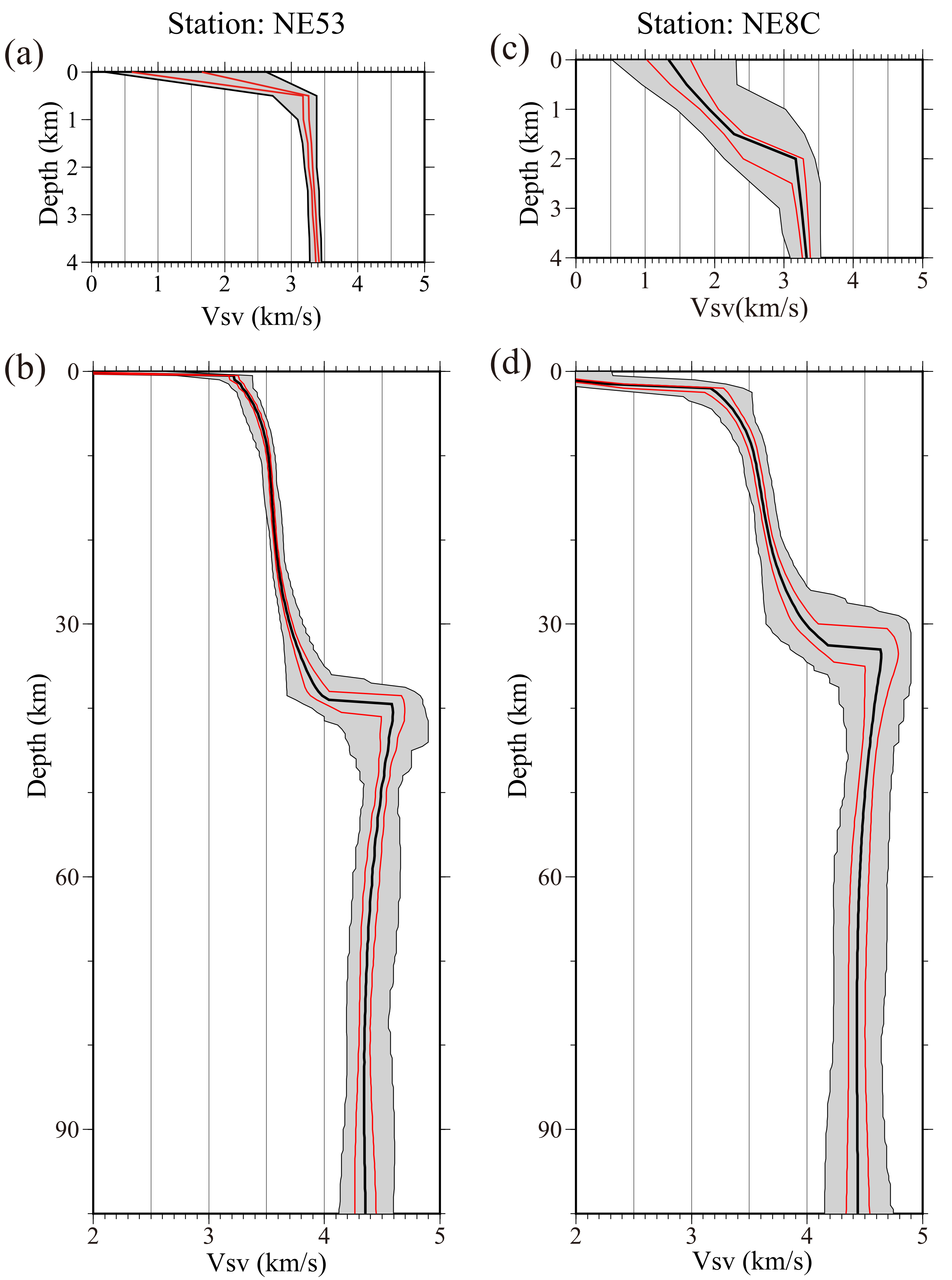

Figure 9

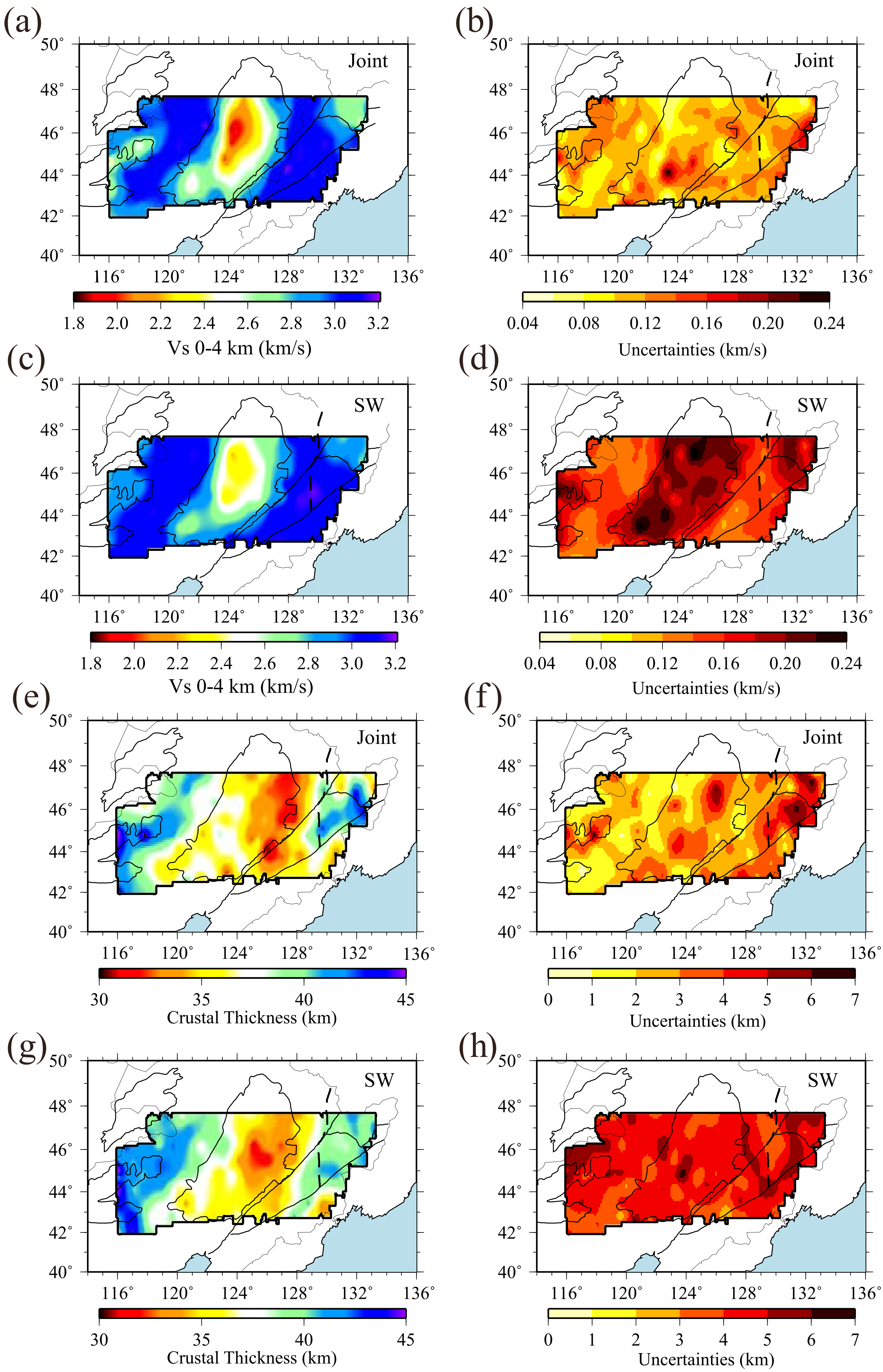
(a)
Joint
Vs 0-4 km (km/s)
1.8 2.0 2.2 2.4 2.6 2.8 3.0 3.2
(b)
Joint
Uncertainties (km/s)
0.04 0.08 0.12 0.16 0.20 0.24
(c)
SW
Vs 0-4 km (km/s)
(d)
SW
Uncertainties (km/s)
(e)
Joint
Crustal Thickness (km)
30 35 40 45
(f)
Joint
Uncertainties (km)
0 1 2 3 4 5 6 7
(g)
SW
Crustal Thickness (km)
(h)
SW
Uncertainties (km)
50° 48° 46° 44° 42° 40°
116° 120° 124° 128° 132° 136°

Figure 10

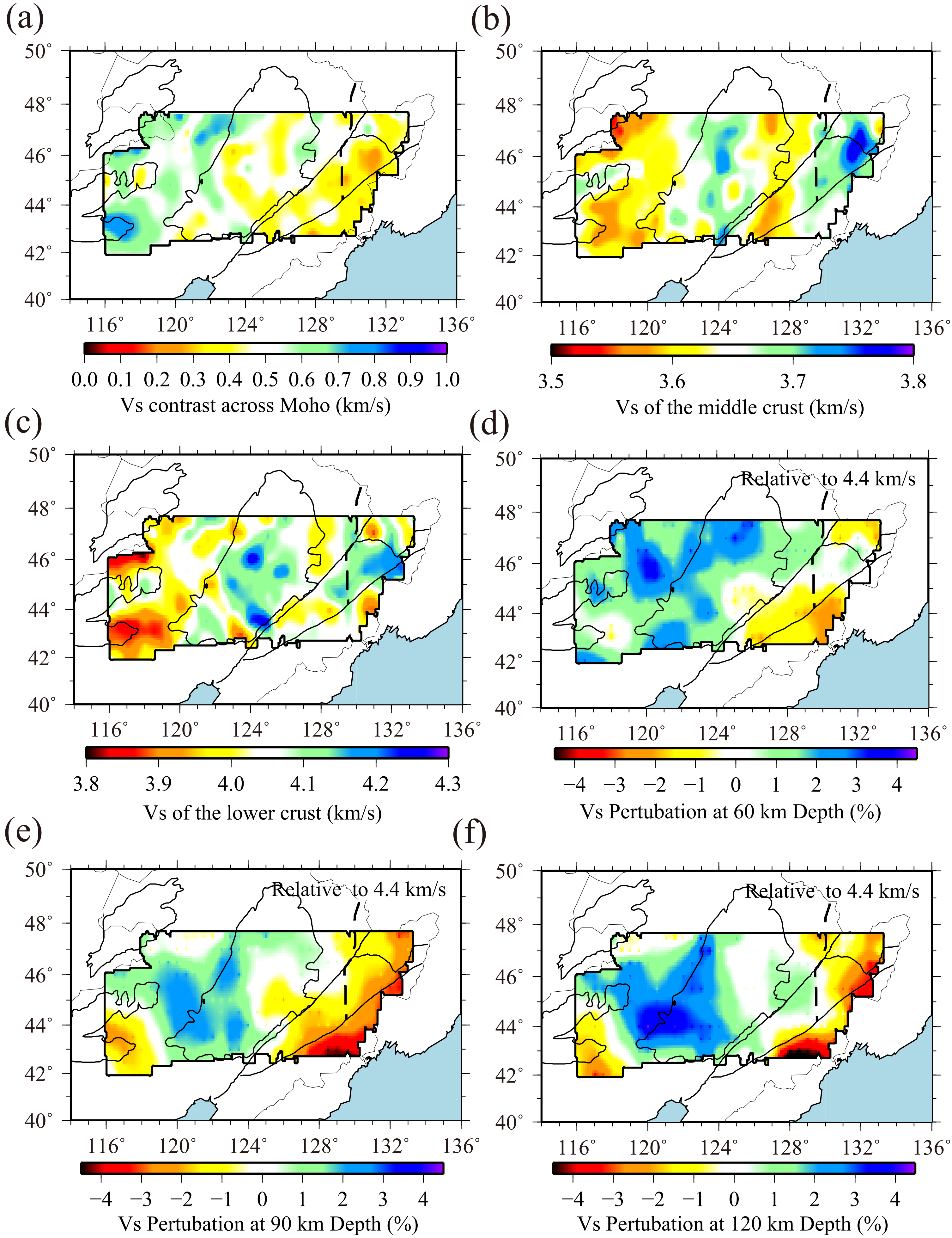
(a)
Vs contrast across Moho (km/s)
(b)
Vs of the middle crust (km/s)
(c)
Vs of the lower crust (km/s)
(d)
Relative to 4.4 km/s
Vs Pertubation at 60 km Depth (%)
(e)
Relative to 4.4 km/s
Vs Pertubation at 90 km Depth (%)
(f)
Relative to 4.4 km/s
Vs Pertubation at 120 km Depth (%)

Figure 11

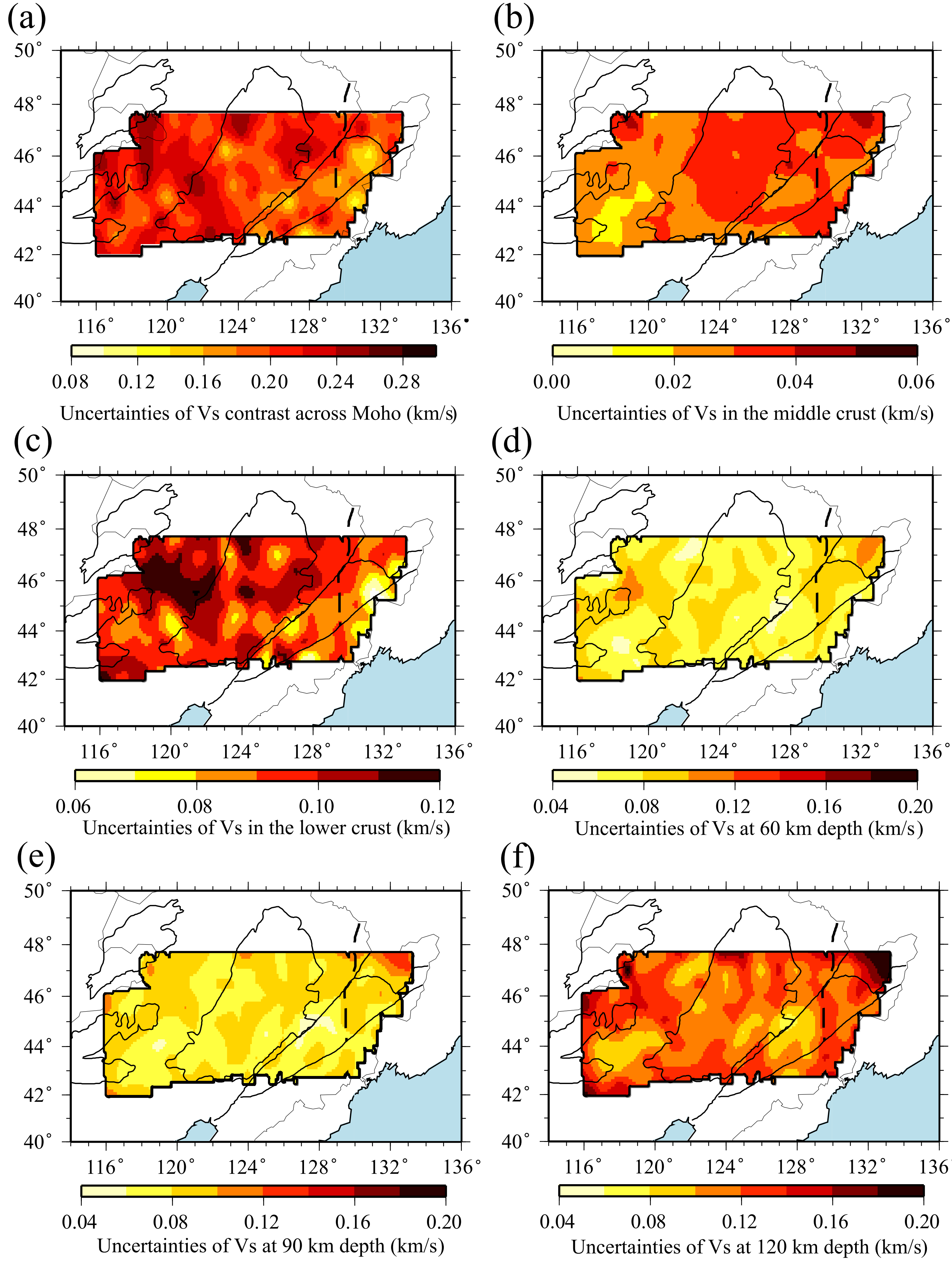
(a)
(b)
Uncertainties of Vs contrast across Moho (km/s)
Uncertainties of Vs in the middle crust (km/s)
(c)
(d)
Uncertainties of Vs in the lower crust (km/s)
Uncertainties of Vs at 60 km depth (km/s)
(e)
(f)
Uncertainties of Vs at 90 km depth (km/s)
Uncertainties of Vs at 120 km depth (km/s)

Figure 12

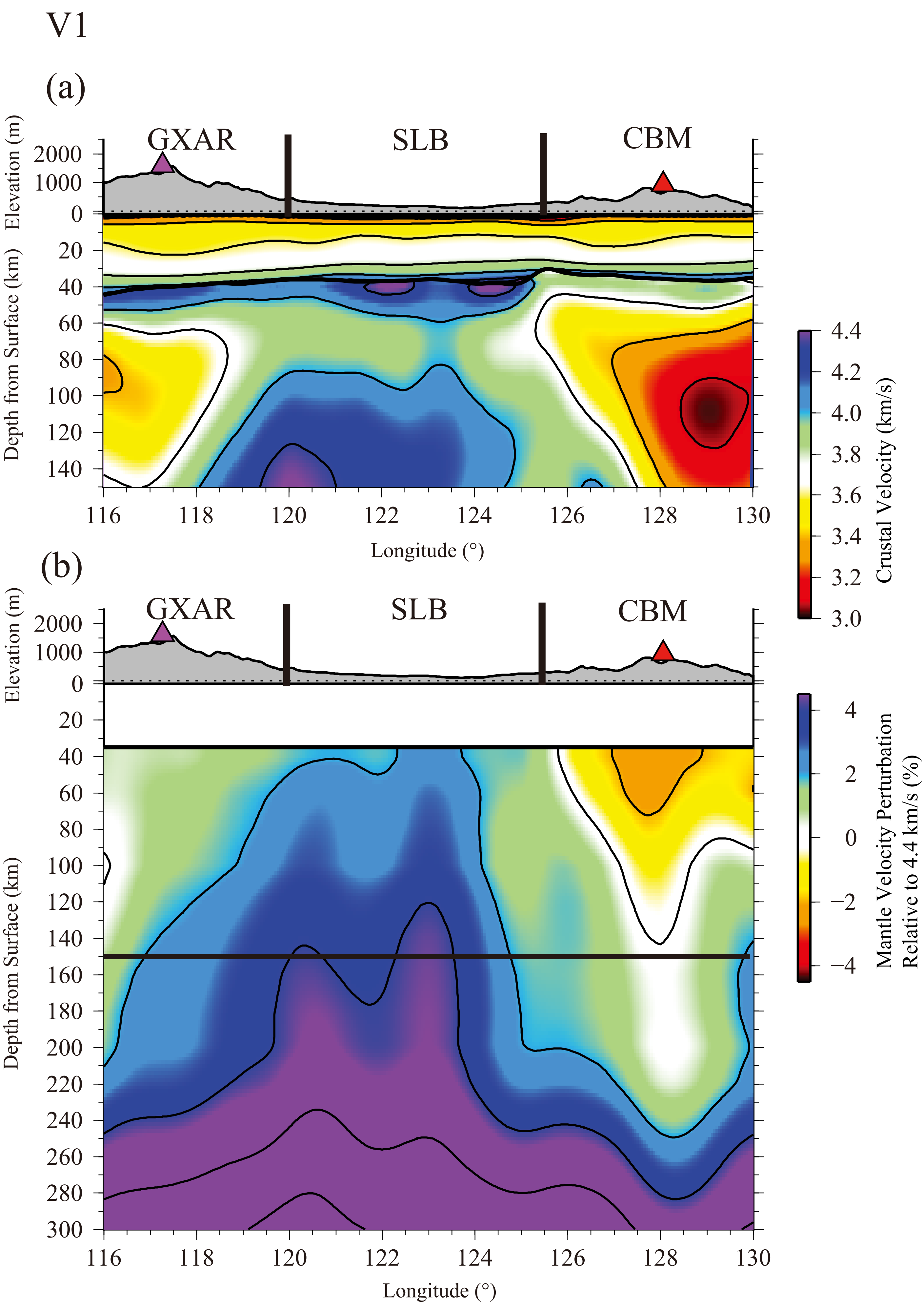
V1
(a)
GXAR
SLB
CBM
Elevation (m)
2000
1000
0
Depth from Surface (km)
20
40
60
80
100
120
140
116
118
120
122
124
126
128
130
Longitude (°)
4.4
4.2
4.0
3.8
3.6
3.4
3.2
3.0
Crustal Velocity (km/s)
(b)
GXAR
SLB
CBM
Elevation (m)
Depth from Surface (km)
300
Longitude (°)
4
2
0
−2
−4
Mantle Velocity Perturbation
Relative to 4.4 km/s (%)

Figure 13

V2

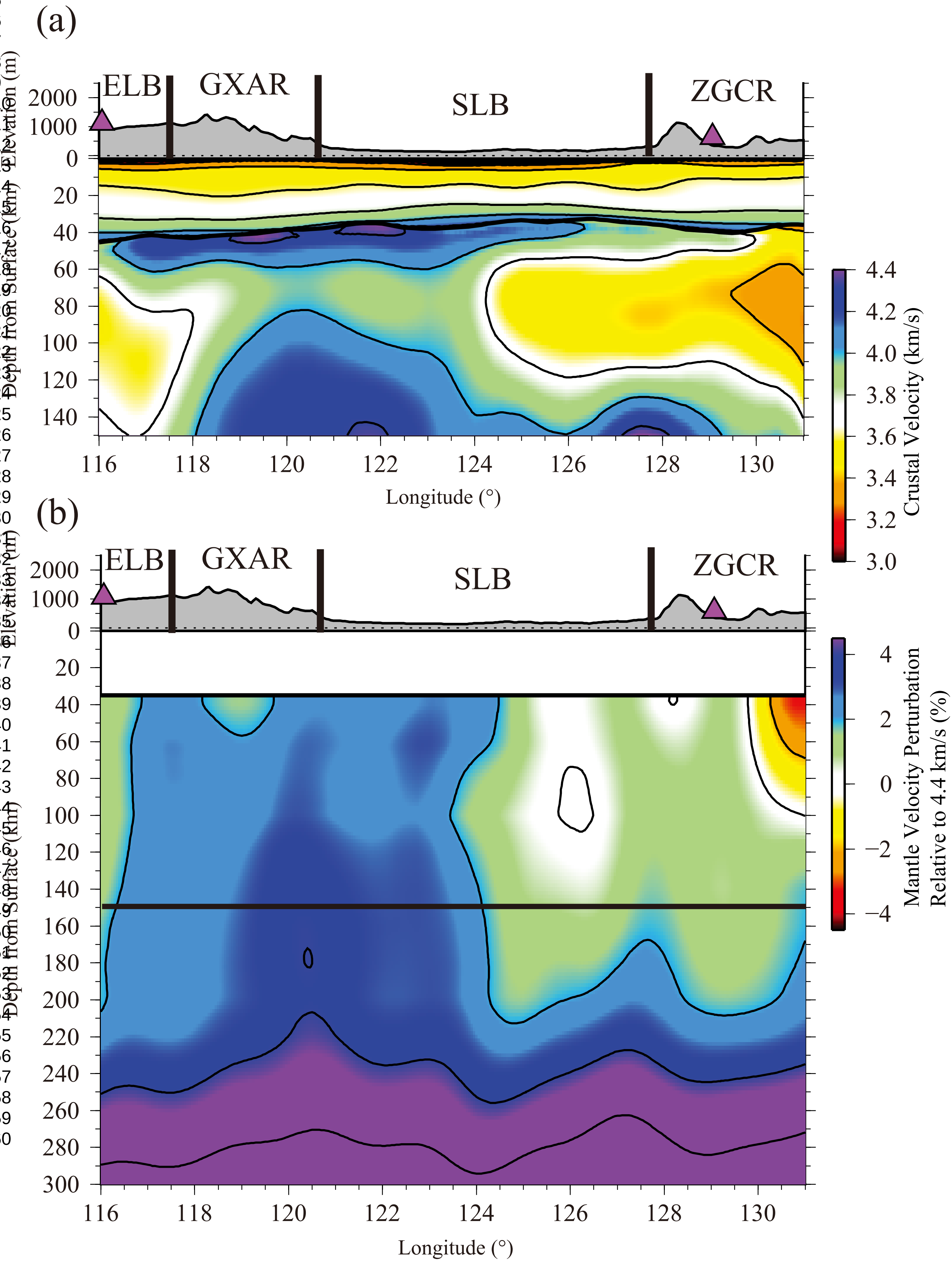
(a)
ELB
GXAR
SLB
ZGCR
Elevation (m)
2000
1000
0
Depth from Surface (km)
20
40
60
80
100
120
140
116
118
120
122
124
126
128
130
Longitude (°)
Crustal Velocity (km/s)
4.4
4.2
4.0
3.8
3.6
3.4
3.2
3.0
(b)
ELB
GXAR
SLB
ZGCR
Elevation (m)
2000
1000
0
Depth from Surface (km)
20
40
60
80
100
120
140
160
180
200
220
240
260
280
300
116
118
120
122
124
126
128
130
Longitude (°)
Mantle Velocity Perturbation
Relative to 4.4 km/s (%)
4
2
0
−2
−4

Figure 14

V3

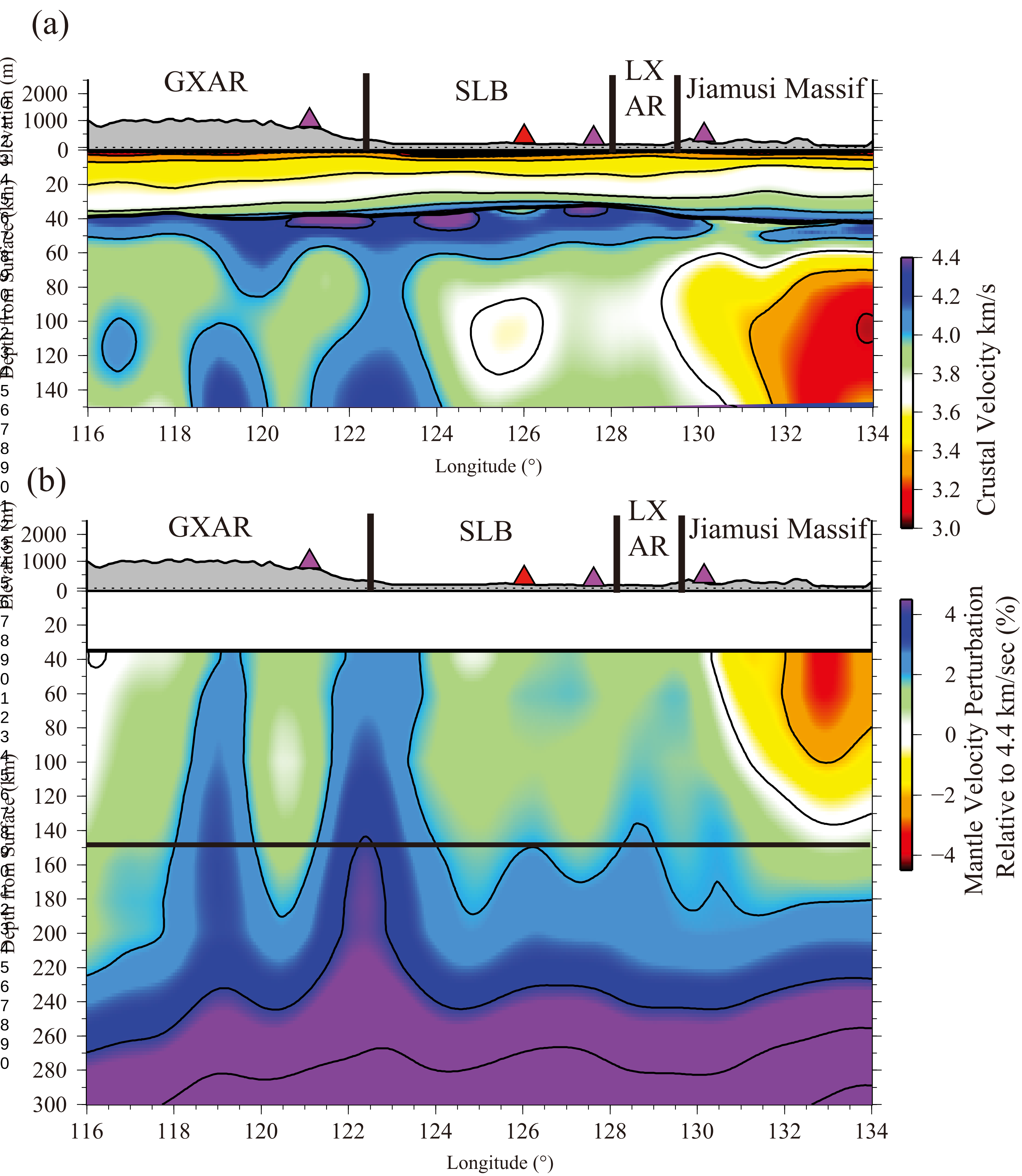
(a)
GXAR
SLB
LX
AR
Jiamusi Massif
Elevation (m)
2000
1000
0
Depth from Surface (km)
20
40
60
80
100
120
140
116
118
120
122
124
126
128
130
132
134
Longitude (°)
Crustal Velocity km/s
4.4
4.2
4.0
3.8
3.6
3.4
3.2
3.0
(b)
GXAR
SLB
LX
AR
Jiamusi Massif
Elevation (m)
2000
1000
0
Depth from Surface (km)
20
40
60
80
100
120
140
160
180
200
220
240
260
280
300
116
118
120
122
124
126
128
130
132
134
Longitude (°)
Mantle Velocity Perturbation
Relative to 4.4 km/sec (%)
4
2
0
−2
−4

Figure 15

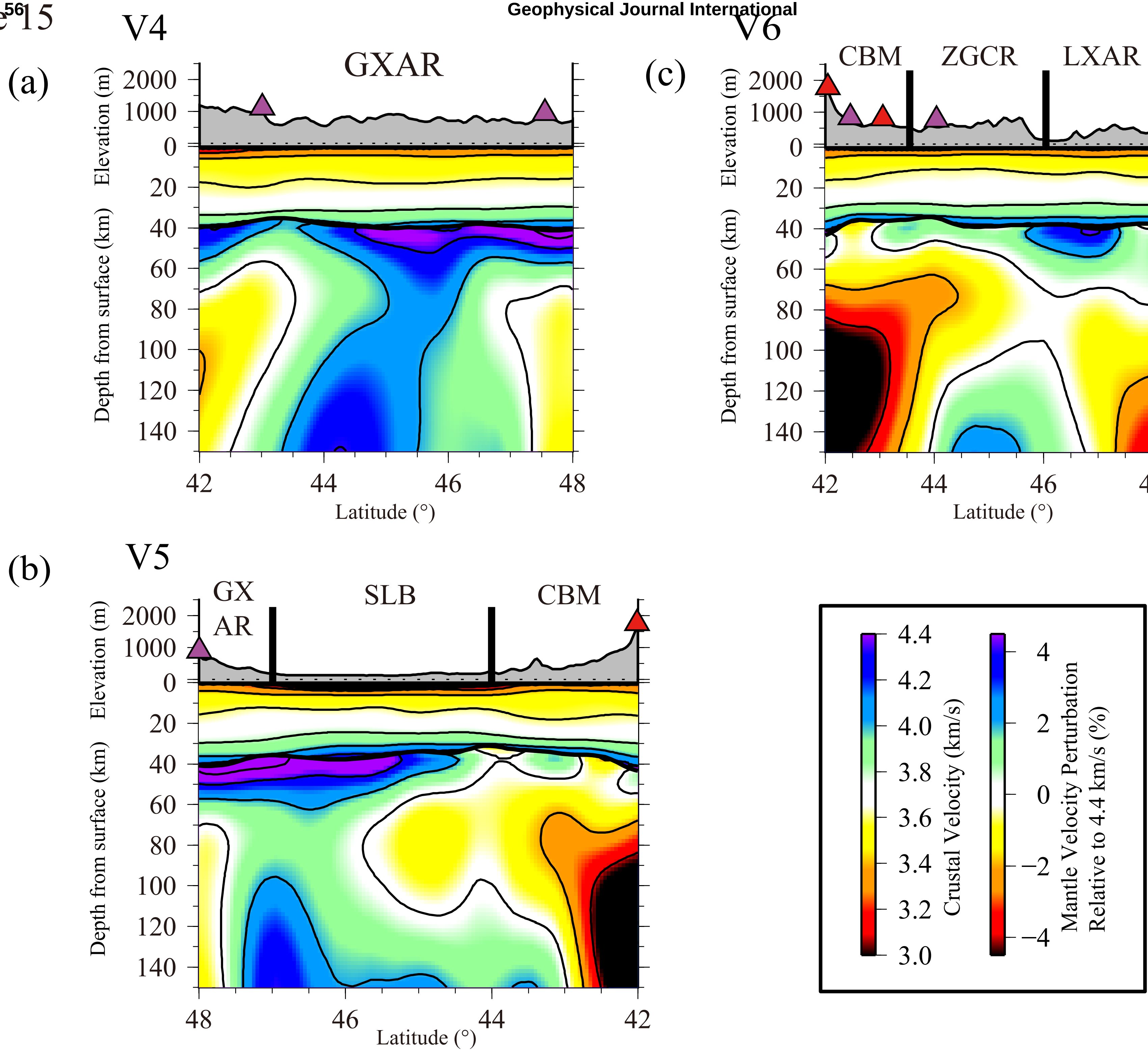
V4
(a)
GXAR
Elevation (m)
Depth from surface (km)
Latitude (°)
V6
(c)
CBM
ZGCR
LXAR
Elevation (m)
Depth from surface (km)
Latitude (°)
V5
(b)
GX
AR
SLB
CBM
Elevation (m)
Depth from surface (km)
Latitude (°)
Crustal Velocity (km/s)
Mantle Velocity Perturbation
Relative to 4.4 km/s (%)

Figure 16

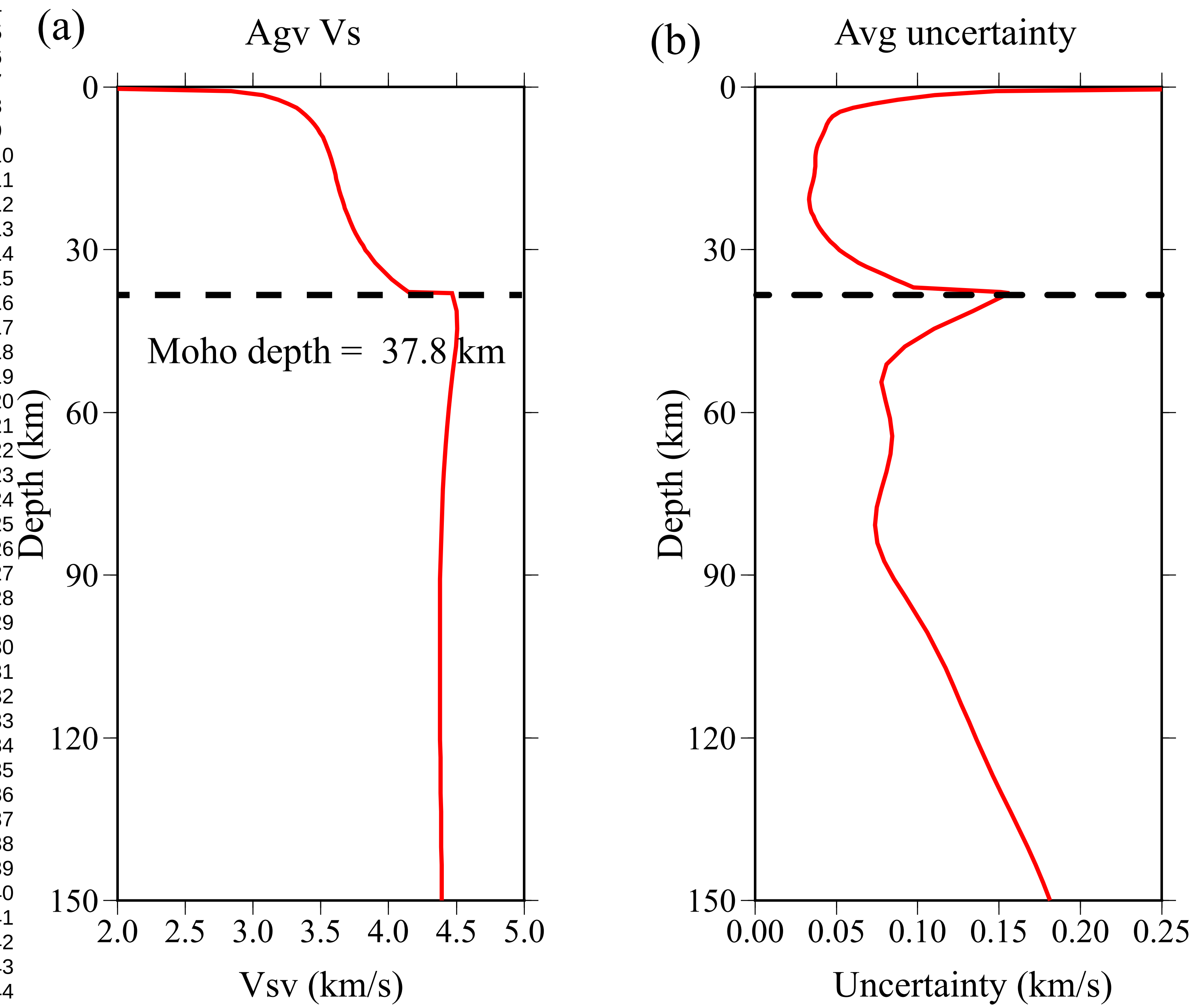
(a)
Agv Vs
0
30
60
90
120
150
Depth (km)
Moho depth = 37.8 km
2.0 2.5 3.0 3.5 4.0 4.5 5.0
Vsv (km/s)
(b)
Avg uncertainty
0
30
60
90
120
150
Depth (km)
0.00 0.05 0.10 0.15 0.20 0.25
Uncertainty (km/s)